1

THE POISSON EQUATION

The Poisson equation

$$-\nabla^2 u = f \tag{1.1}$$

is the simplest and the most famous elliptic partial differential equation. The source (or load) function f is given on some two- or three-dimensional domain denoted by $\Omega \subset \mathbb{R}^2$ or $\mathbb{R}^3$. A solution u satisfying (1.1) will also satisfy boundary conditions on the boundary $\partial\Omega$ of Ω; for example

$$\alpha u + \beta \frac{\partial u}{\partial n} = g \quad \text{on } \partial\Omega, \tag{1.2}$$

where $\partial u/\partial n$ denotes the directional derivative in the direction normal to the boundary $\partial\Omega$ (conventionally pointing outwards) and α and β are constant, although variable coefficients are also possible. In a practical setting, u could represent the temperature field in Ω subject to the external heat source f. Other important physical models include gravitation, electromagnetism, elasticity and inviscid fluid mechanics, see Ockendon et al. [139, chap. 5] for motivation and discussion.

The combination of (1.1) and (1.2) together is referred to as a *boundary value problem*. If the constant β in (1.2) is zero, then the boundary condition is of Dirichlet type, and the boundary value problem is referred to as the Dirichlet problem for the Poisson equation. Alternatively, if the constant α is zero, then we correspondingly have a Neumann boundary condition, and a Neumann problem. A third possibility is that Dirichlet conditions hold on part of the boundary $\partial\Omega_D$, and Neumann conditions (or indeed *mixed* conditions where α and β are both nonzero) hold on the remainder $\partial\Omega \backslash \partial\Omega_D$.

The case $\alpha = 0$, $\beta = 1$ in (1.2) demands special attention. First, since $u =$ constant satisfies the *homogeneous* problem with $f = 0$, $g = 0$, it is clear that a solution to a Neumann problem can only be unique up to an additive constant. Second, integrating (1.1) over Ω using Gauss's theorem gives

$$-\int_{\partial\Omega} \frac{\partial u}{\partial n} = -\int_{\Omega} \nabla^2 u = \int_{\Omega} f; \tag{1.3}$$

thus a necessary condition for the existence of a solution to a Neumann problem is that the source and boundary data satisfy the *compatibility* condition

$$\int_{\partial\Omega} g + \int_{\Omega} f = 0. \tag{1.4}$$

1.1 Reference problems

The following examples of two-dimensional Poisson problems will be used to illustrate the power of the finite element approximation techniques that are developed in the remainder of the chapter. Since these problems are all of Dirichlet type (i.e. the boundary condition associated with (1.1) is of the form $u = g$ on $\partial\Omega$), the problem specification involves the shape of the domain Ω, the source data f and the boundary data g. The examples are posed on one of two domains: a square $\Omega_{\square} = (-1,1) \times (-1,1)$, or an L-shaped domain $\Omega_{\lrcorner}$ consisting of the complement in $\Omega_{\square}$ of the quadrant $(-1,0] \times (-1,0]$.

1.1.1 Example: Square domain $\Omega_{\square}$, constant source function $f(x) \equiv 1$, zero boundary condition.

This problem represents a simple diffusion model for the temperature distribution $u(x,y)$ in a square plate. The specific source term in this example models uniform heating of the plate, and the boundary condition models the edge of the plate being kept at an ice-cold temperature. The simple shape of the domain enables the solution to be explicitly represented. Specifically, using separation of variables it can be shown that

$$u(x,y) = \frac{(1-x^2)}{2} - \frac{16}{\pi^3} \sum_{\substack{k=1 \\ k \text{ odd}}}^{\infty} \left\{ \frac{\sin(k\pi(1+x)/2)}{k^3 \sinh(k\pi)} \right. \\ \left. \times \left(\sinh(k\pi(1+y)/2) + \sinh(k\pi(1-y)/2)\right) \right\}. \tag{1.5}$$

Series solutions of this type can only be found in the case of geometrically simple domains. Moreover, although such solutions are aesthetically pleasing to mathematicians, they are rather less useful in terms of computation. These are the raisons d'etre for approximation strategies such as the finite element method considered in this monograph.

A finite element solution (computed using our IFISS software) approximating the exact solution u is illustrated in Figure 1.1. The accuracy of the computed solution is explored in Computational Exercise 1.1.

1.1.2 Example: L-shaped domain $\Omega_{\lrcorner}$, constant source function $f(x) \equiv 1$, zero boundary condition.

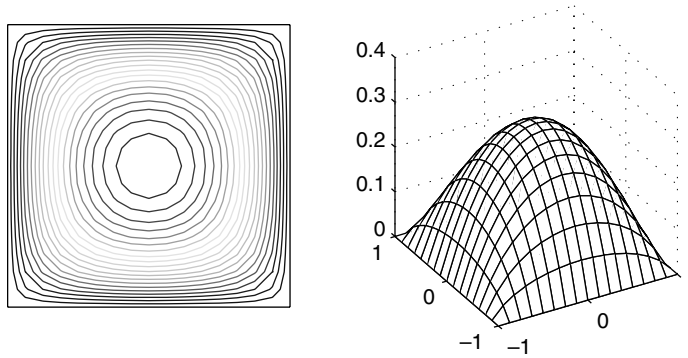

FIG. 1.1. Contour plot (left) and three-dimensional surface plot (right) of a finite element solution of Example 1.1.1.

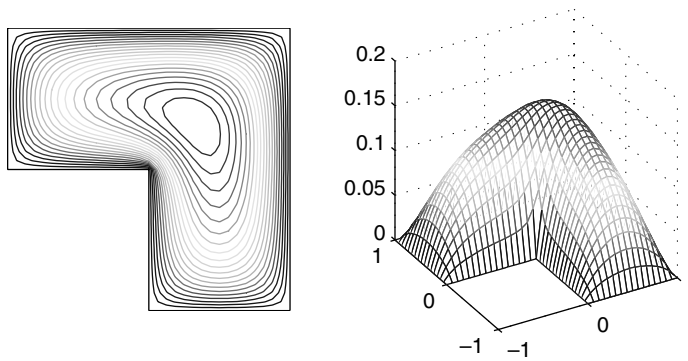

FIG. 1.2. Contour plot (left) and three-dimensional surface plot (right) of a finite element solution of Example 1.1.2.

A typical finite element solution is illustrated in Figure 1.2 (and is again easily computed using our IFISS software, see Computational Exercise 1.2). Notice that the contours are very close together around the corner at the origin, suggesting that the temperature is rapidly varying in this vicinity. A more careful investigation shows that the underlying Poisson problem has a *singularity* — the solution u is closely approximated at the origin by the function

$$u^*_\Gamma(r,\theta) = r^{2/3}\sin((2\theta+\pi)/3), \tag{1.6}$$

where r represents the radial distance from the origin, and θ the angle with the vertical axis. This singular behavior is identified more precisely in Example 1.1.4. Here we simply note that radial derivatives of u^*_Γ (and by implication those of u) are unbounded at the origin. See Strang & Fix [188, chap. 8] for further discussion of this type of function.

In order to assess the accuracy of approximations to the solution of boundary value problems in this and subsequent chapters, it will be convenient to refer to *analytic* test problems — these have an exact solution that can be explicitly computed at all points in the domain. Examples 1.1.3 and 1.1.4 are in this category.

1.1.3 Example: Square domain $\Omega_\square$, analytic solution.

This analytic test problem is associated with the following solution of Laplace's equation (i.e. (1.1) with $f = 0$),

$$u^*(x, y) = \frac{2(1 + y)}{(3 + x)^2 + (1 + y)^2}. \tag{1.7}$$

Note that this function is perfectly smooth since the domain $\Omega_\square$ excludes the point $(-3, -1)$. A finite element approximation to u^* is given in Figure 1.3. For future reference we note that the boundary data g is given by the finite element interpolant of u^* on $\partial\Omega_\square$. We will return to this example when we consider finite element approximation errors in Section 1.5.1.

1.1.4 Example: L-shaped domain $\Omega_\lrcorner$, analytic solution.

This analytic test problem is associated with the singular solution $u^*_\lrcorner$ introduced in Example 1.1.2. A typical finite element approximation to $u^*_\lrcorner$ is given in Figure 1.4. Note that although $u^*_\lrcorner$ satisfies (1.1) with $f = 0$, see Problem 1.1, $u^*_\lrcorner$ is not smooth enough to meet the strict definition of a classical solution given in the next section. We will return to this example when discussing a posteriori error estimation in Section 1.5.2.

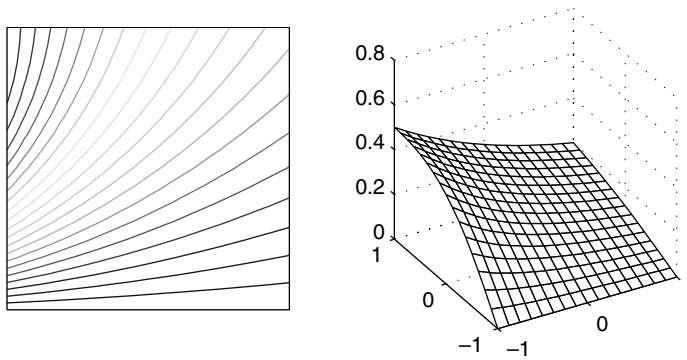

FIG. 1.3. Contour plot (left) and three-dimensional surface plot (right) of a finite element solution of Example 1.1.3.

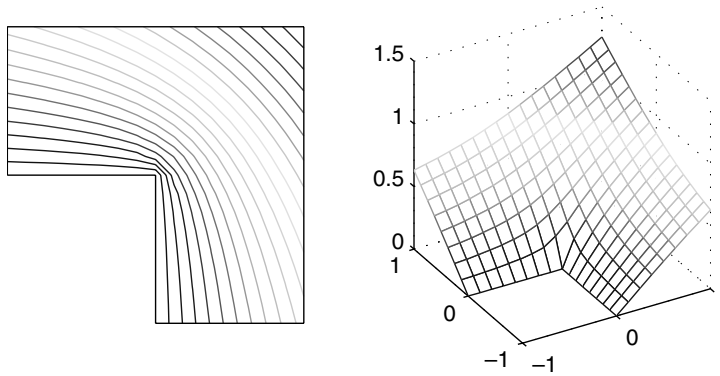

FIG. 1.4. Contour plot (left) and three-dimensional surface plot (right) of a finite element solution of Example 1.1.4.

1.2 Weak formulation

A sufficiently smooth function u satisfying both (1.1) and (1.2) is known as a *classical solution* to the boundary value problem, see Renardy & Rogers [157]. For a Dirichlet problem, u is a classical solution only if it has continuous second derivatives in Ω (i.e. u is in $C^2(\Omega)$) and is continuous up to the boundary (u is in $C^0(\overline{\Omega})$); see Braess [19, p. 34] for further details. In cases of non-smooth domains or discontinuous source functions, the function u satisfying (1.1)–(1.2) may not be smooth (or *regular*) enough to be regarded as a classical solution. As we have observed, on the non-convex domain $\Omega_{\sqsubset}$ of Example 1.1.4, the solution $u^*_{\sqsubset}$ is not a classical solution — in fact it does not even have a square integrable second derivative (see Problem 1.20 and the discussion in Section 1.5.1). Alternatively, suppose that the source function is discontinuous, say $f = 1$ on $\{(x, y) \,|\, 0 < x < 1\} \subset \Omega_{\square}$ and $f = 0$ on $\{(x, y) \,|\, -1 < x < 0\}$, which corresponds to a weight placed on part of an elastic membrane. Since f is discontinuous in the x direction, the second partial derivative of the solution u with respect to x is discontinuous, and hence u cannot be in $C^2(\Omega)$, and there is no classical solution. For such problems, which arise from perfectly reasonable mathematical models, an alternative description of the boundary value problem is required. Since this alternative description is less restrictive in terms of the admissible data it is called a *weak formulation*.

To derive a weak formulation of a Poisson problem, we require that for an appropriate set of *test functions* v,

$$\int_{\Omega} (\nabla^2 u + f)v = 0. \tag{1.8}$$

This formulation exists provided that the integrals are well defined. If u is a classical solution then it must also satisfy (1.8). If v is sufficiently smooth

however, then the smoothness required of u can be reduced by using the derivative of a product rule and the divergence theorem

$$\begin{aligned} -\int_\Omega v\nabla^2 u &= \int_\Omega \nabla u\cdot\nabla v - \int_\Omega \nabla\cdot(v\nabla u)\\ &= \int_\Omega \nabla u\cdot\nabla v - \int_{\partial\Omega} v\frac{\partial u}{\partial n}, \end{aligned}$$

so that

$$\int_\Omega \nabla u\cdot\nabla v = \int_\Omega vf + \int_{\partial\Omega} v\frac{\partial u}{\partial n}. \tag{1.9}$$

The point here is that the Problem (1.9) may have a solution u, called a *weak solution*, that is not smooth enough to be classical solution. If a classical solution does exist then (1.9) is equivalent to (1.1)–(1.2) and the weak solution is classical.

The case of a Neumann problem ($\alpha = 0$, $\beta = 1$ in (1.2)) is particularly straightforward. Substituting (1.2) into (1.9) gives the following formulation: find u defined on Ω such that

$$\int_\Omega \nabla u\cdot\nabla v = \int_\Omega vf + \int_{\partial\Omega} vg \tag{1.10}$$

for all suitable test functions v.

We need to address an important question at this point, namely, in what sense are the weak solution u and the test functions v in (1.10) meaningful? This is essentially a question of *where* to look to find the solution u, and what is meant by "all suitable v". To provide an answer we use the space of functions that are square-integrable in the sense of Lebesgue

$$L_2(\Omega) := \left\{ u : \Omega\to\mathbb{R} \;\middle|\; \int_\Omega u^2 < \infty \right\}, \tag{1.11}$$

and make use of the L_2 measure

$$\|u\| := \left(\int_\Omega u^2\right)^{1/2}. \tag{1.12}$$

The integral on the left-hand side of (1.10) will be well defined if all first derivatives are in $L_2(\Omega)$; for example, if Ω is a two-dimensional domain and $\partial u/\partial x, \partial u/\partial y \in L_2(\Omega)$ with $\partial v/\partial x, \partial v/\partial y \in L_2(\Omega)$, then using the

Cauchy–Schwarz inequality,

$$\int_\Omega \nabla u \cdot \nabla v = \int_\Omega \left(\frac{\partial u}{\partial x}\right)\left(\frac{\partial v}{\partial x}\right) + \int_\Omega \left(\frac{\partial u}{\partial y}\right)\left(\frac{\partial v}{\partial y}\right)$$
$$\leq \left\|\frac{\partial u}{\partial x}\right\| \left\|\frac{\partial v}{\partial x}\right\| + \left\|\frac{\partial u}{\partial y}\right\| \left\|\frac{\partial v}{\partial y}\right\| < \infty.$$

Similarly, the integrals on the right-hand side of (1.10) will certainly be well-defined if $f \in L_2(\Omega)$ and $g \in L_2(\partial\Omega)$.[1]

To summarize, if $\Omega \subset \mathbb{R}^2$ then the *Sobolev space* $\mathcal{H}^1(\Omega)$ given by

$$\mathcal{H}^1(\Omega) := \left\{ u : \Omega \to \mathbb{R} \,\middle|\, u, \frac{\partial u}{\partial x}, \frac{\partial u}{\partial y} \in L_2(\Omega) \right\}$$

is the space where a weak solution of (1.10) naturally exists, and this space is also the natural home for the test functions v. For clarity of exposition, further discussion of such technical issues is postponed until Section 1.5.

We now return to (1.9) and consider other types of boundary conditions. In general, we only need to look for weak solutions among those functions that satisfy the Dirichlet boundary conditions. (Engineers call Dirichlet boundary conditions "essential conditions" whereas Neumann conditions are "natural conditions" for the Laplacian.) To fix ideas, in the remainder of the chapter we restrict our attention to the following generic boundary value problem:

Find u such that

$$-\nabla^2 u = f \quad \text{in } \Omega \tag{1.13}$$

$$u = g_D \text{ on } \partial\Omega_D \quad \text{and} \quad \frac{\partial u}{\partial n} = g_N \text{ on } \partial\Omega_N, \tag{1.14}$$

where $\partial\Omega_D \cup \partial\Omega_N = \partial\Omega$ and $\partial\Omega_D$ and $\partial\Omega_N$ are distinct.

We assume that $\int_{\partial\Omega_D} \mathrm{d}s \neq 0$, so that (1.14) does not represent a Neumann condition. Then we define *solution* and *test* spaces by

$$\mathcal{H}^1_E := \{u \in \mathcal{H}^1(\Omega) \,|\, u = g_D \text{ on } \partial\Omega_D\}, \tag{1.15}$$

$$\mathcal{H}^1_{E_0} := \{v \in \mathcal{H}^1(\Omega) \,|\, v = 0 \text{ on } \partial\Omega_D\}, \tag{1.16}$$

respectively. We should emphasize the difference between the two spaces: the Dirichlet condition from (1.14) is built into the definition of the solution space $\mathcal{H}^1_E$, whereas functions in the test space $\mathcal{H}^1_{E_0}$ are zero on the Dirichlet portion of the boundary. This is in contrast to the Neumann case where the solution and

[1]The boundary term can be shown to be well-defined using the *trace inequality* given in Lemma 1.5 in Section 1.5.1.

the test functions are not restricted on the boundary. Notice that the solution space is not closed under addition so strictly speaking it is not a vector space.

From (1.9) it is clear that any function u that satisfies (1.13) and (1.14) is also a solution of the following weak formulation:

Find $u \in \mathcal{H}^1_E$ such that

$$\int_\Omega \nabla u \cdot \nabla v = \int_\Omega vf + \int_{\partial\Omega_N} vg_N \quad \text{for all } v \in \mathcal{H}^1_{E_0}. \tag{1.17}$$

We reiterate a key point here; a classical solution of a Poisson problem has to be twice differentiable in Ω — this is a much more stringent requirement than square integrability of first derivatives. Using (1.17) instead as the starting point enables us to look for approximate solutions that only need satisfy the smoothness requirement and the essential boundary condition embodied in (1.15). The case of a Poisson problem with a mixed boundary condition (1.2) is explored in Problem 1.2.

1.3 The Galerkin finite element method

We now develop the idea of approximating u by taking a finite-dimensional subspace of the solution space $\mathcal{H}^1_E$. The starting point is the weak formulation (1.15)–(1.17) of the generic problem (1.13)–(1.14). To construct an approximation method, we assume that $S^h_0 \subset \mathcal{H}^1_{E_0}$ is a finite n-dimensional vector space of test functions for which $\{\phi_1, \phi_2, \ldots, \phi_n\}$ is a convenient basis. Then, in order to ensure that the Dirichlet boundary condition in (1.15) is satisfied, we extend this basis set by defining additional functions $\phi_{n+1}, \ldots, \phi_{n+n_\partial}$ and select fixed coefficients $\mathbf{u}_j, j = n+1, \ldots, n+n_\partial$, so that the function $\sum_{j=n+1}^{n+n_\partial} \mathbf{u}_j\phi_j$ interpolates the boundary data g_D on $\partial\Omega_D$. The finite element approximation $u_h \in S^h_E$ is then uniquely associated with the vector $\mathbf{u} = (\mathbf{u}_1, \mathbf{u}_2, \ldots, \mathbf{u}_n)^T$ of real coefficients in the expansion

$$u_h = \sum_{j=1}^{n} \mathbf{u}_j\phi_j + \sum_{j=n+1}^{n+n_\partial} \mathbf{u}_j\phi_j. \tag{1.18}$$

The functions $\phi_i, i = 1, \ldots, n$ in the first sum in (1.18) define a set of *trial functions*. (In a finite element context they are often called *shape* functions.)

The construction (1.18) cleverly simplifies the characterization of discrete solutions when faced with difficult-to-satisfy essential boundary data,[2] for example, when solving test problems like that in Example 1.1.3.

[2]But it complicates the error analysis, see Section 1.5; if the data g_D is approximated then $S^h_E \not\subset \mathcal{H}^1_E$.

The construction of the space S_E^h is achieved above by ensuring that the specific choice of trial functions in (1.18) coincides with the choice of test functions that form the basis for S_0^h, and is generally referred to as the *Galerkin* (or more precisely *Bubnov–Galerkin*) approximation method. A more general approach is to construct approximation spaces for (1.15) and (1.16) using different trial and test functions. This alternative is called a *Petrov–Galerkin* approximation method, and a specific example will be discussed in Chapter 3.

The result of the Galerkin approximation is a finite-dimensional version of the weak formulation: find $u_h \in S_E^h$ such that

$$\int_\Omega \nabla u_h \cdot \nabla v_h = \int_\Omega v_h f + \int_{\partial\Omega_N} v_h g_N \quad \text{for all } v_h \in S_0^h. \tag{1.19}$$

For computations, it is convenient to enforce (1.19) for each basis function; then it follows from (1.18) that (1.19) is equivalent to finding $\mathbf{u}_j, j = 1, \ldots, n$ such that

$$\sum_{j=1}^{n} \mathbf{u}_j \int_\Omega \nabla\phi_j \cdot \nabla\phi_i = \int_\Omega \phi_i f \; + \int_{\partial\Omega_N} \phi_i g_N \; - \sum_{j=n+1}^{n+n_\partial} \mathbf{u}_j \int_\Omega \nabla\phi_j \cdot \nabla\phi_i \tag{1.20}$$

for $i = 1, \ldots, n$. This can be written in matrix form as the linear system of equations

$$A\mathbf{u} = \mathbf{f} \tag{1.21}$$

with

$$A = [a_{ij}], \quad a_{ij} = \int_\Omega \nabla\phi_j \cdot \nabla\phi_i, \tag{1.22}$$

and

$$\mathbf{f} = [\boldsymbol{f}_i], \qquad \boldsymbol{f}_i = \int_\Omega \phi_i f + \int_{\partial\Omega_N} \phi_i g_N \; - \sum_{j=n+1}^{n+n_\partial} \mathbf{u}_j \int_\Omega \nabla\phi_j \cdot \nabla\phi_i. \tag{1.23}$$

The system of linear equations (1.21) is called the *Galerkin system*, and the function u_h computed by substituting the solution of (1.21) into (1.18) is the *Galerkin solution*. The matrix A is also referred to as the *stiffness matrix*.

The Galerkin coefficient matrix (1.22) is clearly symmetric (in contrast, using different test and trial functions necessarily leads to a nonsymmetric system matrix), and it is also positive-definite. To see this, consider a general coefficient

vector $\mathbf{v}$ corresponding to a specific function $v_h = \sum_{j=1}^n \mathbf{v}_j \phi_j \in S_0^h$, so that

$$\begin{aligned}
\mathbf{v}^T A \mathbf{v} &= \sum_{j=1}^n \sum_{i=1}^n \mathbf{v}_j a_{ji} \mathbf{v}_i \\
&= \sum_{j=1}^n \sum_{i=1}^n \mathbf{v}_j \left(\int_\Omega \nabla \phi_j \cdot \nabla \phi_i \right) \mathbf{v}_i \\
&= \int_\Omega \left(\sum_{j=1}^n \mathbf{v}_j \nabla \phi_j \right) \cdot \left(\sum_{i=1}^n \mathbf{v}_i \nabla \phi_i \right) \\
&= \int_\Omega \nabla v_h \cdot \nabla v_h \\
&\geq 0.
\end{aligned}$$

Thus we see that A is at least semi-definite. Definiteness follows from the fact that $\mathbf{v}^T A \mathbf{v} = 0$ if and only if $\nabla v_h = 0$, that is, if and only if v_h is constant in Ω. Since $v_h \in S_0^h$, it is continuous up to the boundary and is zero on $\partial\Omega_D$, thus $\nabla v_h = 0$ implies $v_h = 0$. Finally, since the test functions are a basis for S_0^h we have that $v_h = 0$ implies $\mathbf{v} = \mathbf{0}$.

Once again the Neumann problem (1.10) requires special consideration. The Galerkin matrix is only semi-definite in this case and has a null space of vectors $\mathbf{v}$ corresponding to functions $\nabla v_h = 0$. In this situation it is essential to constrain the subspace $S_h \subset \mathcal{H}^1$ by choosing a set of trial functions $\{\phi_j\}, j = 1, \ldots, n$ that define a *partition of unity*, that is, every vector in S_h must be associated with a coefficient vector $v_h = \sum_{j=1}^n \mathbf{v}_j \phi_j$ satisfying

$$\sum_{j=1}^n \phi_j = 1. \tag{1.24}$$

The construction (1.24) ensures that if v_h is a constant function, say $v_h \equiv \alpha$, then v_h is associated with a discrete vector that satisfies $\mathbf{v}_j = \alpha$ for all the coefficients. This means that the null space of the Galerkin matrix associated with (1.10) is one-dimensional, consisting of constant coefficient vectors. Notice that the solvability of the discrete Neumann system (the analogue of (1.21)) requires that the null space of the Galerkin matrix A be orthogonal to the right-hand side vector $\mathbf{f}$, that is, we require that $(1, \ldots, 1)^T \mathbf{f} = 0$ with

$$\mathbf{f} = [\boldsymbol{f}_i], \qquad \boldsymbol{f}_i = \int_\Omega \phi_i f + \int_{\partial\Omega} \phi_i g. \tag{1.25}$$

Using the property (1.24) shows that the discrete Neumann problem is solvable if and only if the underlying boundary value problem is well posed in the sense that (1.4) holds.

Returning to the general case (1.19), it is clear that the choices of S_E^h and S_0^h are central in that they determine whether or not u_h has any relation to the weak solution u. The inclusions $S_E^h \subset \mathcal{H}_E^1$ and $S_0^h \subset \mathcal{H}_{E_0}^1$ lead to *conforming* approximations; more general *nonconforming* approximation spaces containing specific discontinuous functions are also possible, see for example [19, pp. 104–106], but these are not considered here. The general desire is to choose S_E^h and S_0^h so that approximation to any required accuracy can be achieved if the dimension n is large enough. That is, it is required that the error $\|u - u_h\|$ reduces rapidly as n is increased, and moreover that the computational effort associated with solving (1.21) is acceptable — the choice of basis is critical in this respect. These issues are addressed in Section 1.5 and in Chapter 2.

The mathematical motivation for finite element approximation is the observation that a smooth function can often be approximated to arbitrary accuracy using *piecewise polynomials*. Starting from the Galerkin system (1.19), the idea is to choose basis functions $\{\phi_j\}$ in (1.18) that are locally nonzero on a mesh of triangles ($\mathbb{R}^2$) or tetrahedra ($\mathbb{R}^3$) or a grid of rectangles or bricks. We discuss two-dimensional elements first.

1.3.1 *Triangular finite elements* ($\mathbb{R}^2$)

For simplicity, we assume that $\Omega \subset \mathbb{R}^2$ is polygonal (as is often the case in practice), so that we are able to *tile* (or *tessellate*) the domain with a set of triangles $\triangle_k, k = 1, \ldots, K$, defining a *triangulation* $\mathcal{T}_h$. This means that vertices of neighboring triangles coincide and that

- $\bigcup_k \overline{\triangle}_k = \overline{\Omega}$,
- $\triangle_\ell \cap \triangle_m = \emptyset$ for $\ell \neq m$.

The points where triangle vertices meet are called *nodes*. Surrounding any node is a *patch* of triangles that each have that node as a vertex (see Figure 1.5). If we label the nodes $j = 1, \ldots, n$, then for each j, we define a basis function ϕ_j that is nonzero only on that patch. The simplest choice here (leading to a conforming approximation) is the $\boldsymbol{P}_1$ or piecewise linear basis function: ϕ_j is a linear function on each triangle, which takes the value one at the node point j and zero at all other node points on the mesh. Notice that ϕ_j is clearly continuous on Ω (see Figure 1.6). Moreover, although ϕ_j has discontinuities in slope across element boundaries, it is smooth enough that $\phi_j \in \mathcal{H}^1(\Omega)$, and so it leads to a conforming approximation space $S_0^h = \text{span}(\phi_1, \phi_2, \ldots, \phi_n)$ for use with (1.19).

In terms of approximation, the precise choice of basis for the space is not important; for practical application however, the availability of a locally defined basis such as this one is crucial. Having only three basis functions that are not identically zero on a given triangle means that the construction of the Galerkin

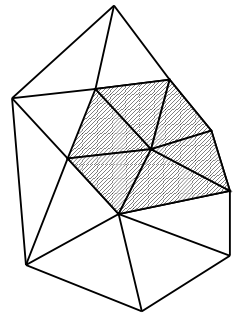

FIG. 1.5. A triangular mesh with a patch shaded.

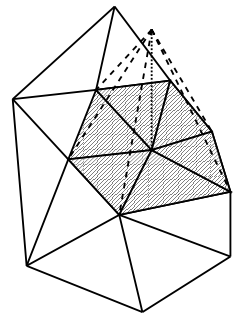

FIG. 1.6. A $\boldsymbol{P}_1$ basis function.

matrix A in (1.21) is easily automated. Another important point is that the Galerkin matrix has a well-defined *sparse* structure: $a_{ij} \neq 0$ only if the node points labeled i and j lie on the same edge of a triangular element. This is important for the development of efficient methods for solving the linear system (1.21), see Chapter 2.

Summarizing, $\boldsymbol{P}_1$ approximation can be characterized by saying that the overall approximation is continuous, and that on any element with vertices i, j and k there are only the three basis functions ϕ_i, ϕ_j and ϕ_k that are not identically zero. Within an element, ϕ_i is a linear function that takes the value one at node i and zero at nodes j and k . This local characterization is convenient for implementation of the finite element method (see Section 1.4) and it is also useful for the description of piecewise polynomial approximation spaces of higher degree.

For piecewise quadratic (or $\boldsymbol{P}_2$) approximation it is convenient to introduce additional nodes at the midpoint of each edge. Thus on each triangle there are six nodes, giving six basis functions that are not identically zero (recall that quadratic functions are of the form $ax^2 + bxy + cy^2 + dx + ey + f$ and thus have six coefficients). As in the linear case, we choose basis functions that have the

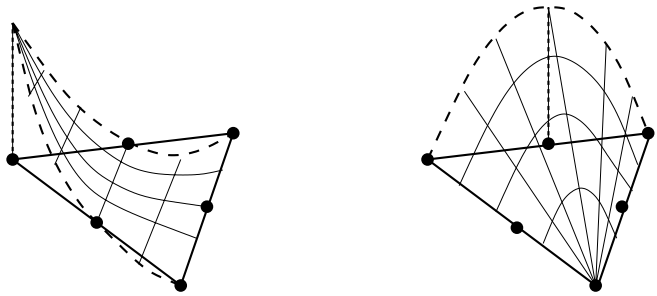

FIG. 1.7. $\boldsymbol{P}_2$ basis functions of vertex type (left) and edge type (right).

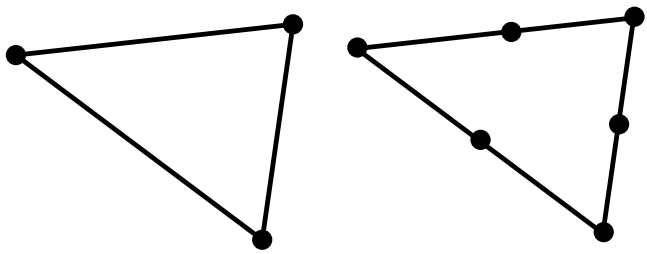

FIG. 1.8. Representation of $\boldsymbol{P}_1$ (left) and $\boldsymbol{P}_2$ (right) elements.

value one at a single node and zero at the other nodes as illustrated in Figure 1.7, see also Problem 1.3. These define a global approximation space of piecewise quadratic functions on the triangulation $\mathcal{T}_h$. Note that there are now "edge" as well as "vertex" functions, and that continuity across edges is guaranteed since there is a unique univariate quadratic (parabola) that takes given values at three points.

The illustration in Figure 1.8 is a convenient way to represent the $\boldsymbol{P}_1$ and $\boldsymbol{P}_2$ triangular elements. In Section 1.5 we will show that there can be advantages in the use of higher order approximations, in terms of the accuracy of approximation. The construction of higher order approximations ($\boldsymbol{P}_m$ with $m \geq 3$) is a straightforward generalization, see [19, pp. 65ff].

1.3.2 *Quadrilateral elements* ($\mathbb{R}^2$)

Although they are less flexible than triangle elements, it is often convenient to consider grids made up of rectangular (or more general quadrilateral) elements. For the simplest domains such as $\Omega_\square$ or $\Omega_\square$ in Section 1.1, it is clearly trivial to tile using square or rectangular elements. For more general domains, it is possible to use rectangles in the interior and then use triangles to match up to the boundary.

The simplest conforming quadrilateral element for a Poisson problem is the bilinear $\boldsymbol{Q}_1$ element defined as follows. On a rectangle, each function is of the

form $(ax+b)(cy+d)$ (hence bilinear). Again, for each of the four basis functions ϕ_j that are not identically zero on an element, the four coefficients are defined by the conditions that ϕ_j has the value one at vertex j and zero at all other vertices. For example, on an element $x \in [0,h]$, $y \in [0,h]$ the *element basis functions* are

$$(1-x/h)(1-y/h), \quad x/h(1-y/h), \quad xy/h^2, \quad (1-x/h)y/h,$$

starting with the function that is one at the origin and then moving anticlockwise. The global basis function on a patch of four elements is shown in Figure 1.9. Note that the $\boldsymbol{Q}_1$ element has the additional "twist" term xy, which is not present in the $\boldsymbol{P}_1$ triangle, and this generally gives the approximate solution some nonzero curvature on each element. Notice however, that when restricted to an edge the $\boldsymbol{Q}_1$ element behaves like the $\boldsymbol{P}_1$ triangle since it varies linearly. In both cases the approximation is continuous but has a discontinuous normal derivative. The upshot is that the $\boldsymbol{Q}_1$ rectangle is in $\mathcal{H}^1(\Omega)$ and is hence conforming for (1.19).

In the case of arbitrary quadrilaterals, straightforward bilinear approximation as described above does not lead to a conforming approximation. A bilinear function is generally quadratic along an edge that is not aligned with a coordinate axis, and so it is not uniquely defined by its value at the two end points. This difficulty can be overcome by defining the approximation through an *isoparametric transformation*. The idea is to define the element basis functions

$$\begin{aligned} \chi_1(\xi,\eta) &= (\xi-1)(\eta-1)/4 \\ \chi_2(\xi,\eta) &= -(\xi+1)(\eta-1)/4 \\ \chi_3(\xi,\eta) &= (\xi+1)(\eta+1)/4 \\ \chi_4(\xi,\eta) &= -(\xi-1)(\eta+1)/4 \end{aligned} \tag{1.26}$$

on a *reference* element $\xi \in [-1,1]$, $\eta \in [-1,1]$, and then to map to any general quadrilateral with vertex coordinates (x_ν, y_ν), $\nu = 1,2,3,4$ by the change

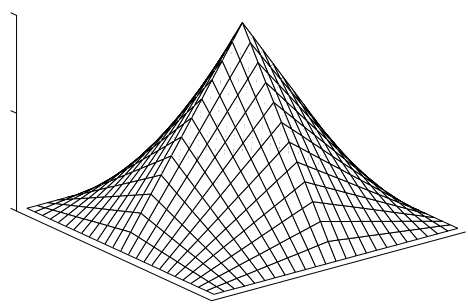

FIG. 1.9. A typical $\boldsymbol{Q}_1$ basis function.

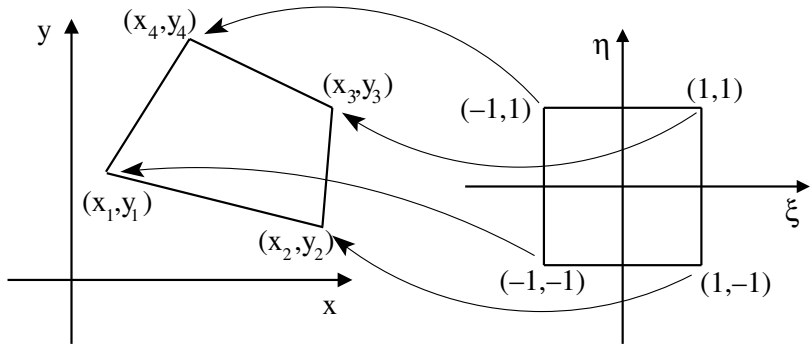

FIG. 1.10. Isoparametric mapping of $\boldsymbol{Q}_1$ element.

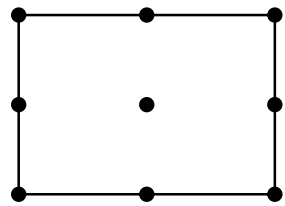

FIG. 1.11. Representation of $\boldsymbol{Q}_2$ element.

of variables

$$x(\xi,\eta)=\sum_{\nu=1}^{4} x_\nu \chi_\nu(\xi,\eta), \quad y(\xi,\eta)=\sum_{\nu=1}^{4} y_\nu \chi_\nu(\xi,\eta), \tag{1.27}$$

see Figure 1.10. The outcome is that the mapped element basis function defined on the general element through (1.27) is linear along each element edge, and so it will connect continuously to the adjacent quadrilateral element whose basis will be defined isoparametrically based on its own vertex positions, see Problem 1.4. Element mappings are more fully discussed in Section 1.4. Notice that when using triangles one could employ a similar isoparametric transformation to a reference triangle based on the $\boldsymbol{P}_1$ basis, see Section 1.4.1 for details.

Higher order approximations are defined analogously. For example, we can define a biquadratic finite element approximation on rectangles by introducing four additional mid-side node points, together with a ninth node at the centroid, as illustrated in the pictorial representation of Figure 1.11. In this case there are four vertex functions, four edge functions and one internal (or *bubble*) function in the element basis. The resulting approximation — which on each rectangle is of the form $(ax^2+bx+c)(dy^2+ey+f)$ — is a linear combination of the nine terms $1, x, y, x^2, xy, y^2, x^2y, xy^2, x^2y^2$ and is called $\boldsymbol{Q}_2$. Note that just as $\boldsymbol{Q}_1$ approximation is a complete linear polynomial together with the xy term of a

bivariate quadratic, $\boldsymbol{Q}_2$ has all six terms of a complete quadratic plus the two cubic terms x^2y, xy^2 and the single quartic term x^2y^2.

Clearly $\boldsymbol{Q}_2$ approximation on rectangles is continuous (for exactly the same reason as $\boldsymbol{P}_2$) and so is conforming for (1.19). $\boldsymbol{Q}_2$ approximation may also be employed on arbitrary quadrilaterals through use of the bilinear mapping (1.27) (in which case the mapping is *subparametric*). Another point worth noting is that triangles and quadrilaterals may be used together in a conforming approximation space. For example, $\boldsymbol{P}_2$ and $\boldsymbol{Q}_2$ both have quadratic variation along edges and so can be used together.

Higher-degree piecewise polynomials may also be defined on rectangles (and thus on quadrilaterals) but other possibilities also present themselves; for example, by excluding the centroid node one is left with eight degrees of freedom, which allows the construction of a basis including all $\boldsymbol{Q}_2$ terms except for the x^2y^2 term, see for example [19, pp. 66ff]. Such an element is a member of the "serendipity" family.

1.3.3 *Tetrahedral elements* ($\mathbb{R}^3$)

The natural counterpart to triangular elements in three dimensions are tetrahedral (or simplex) elements. Any polyhedral region $\Omega \subset \mathbb{R}^3$ can be completely filled with tetrahedra $\triangle_k$ where each triangular face is common to only two tetrahedra, or else is part of the boundary $\partial\Omega$. Thus in a manner analogous to how triangles are treated, we define nodes at the vertices of the faces of the tetrahedra, and we define a $\boldsymbol{P}_1$ basis function ϕ_j that is only nonzero on the set of tetrahedra for which node j is a vertex of one of its faces.

For each node j in a tessellation of Ω, we define $\phi_j(x, y, z)$ to be a linear function (i.e. of the form $a + bx + cy + dz$) on each tetrahedral element satisfying the interpolation condition

$$\phi_j(\text{node } i) = \begin{cases} 1 & \text{when } i = j, \\ 0 & \text{when } i \neq j. \end{cases} \tag{1.28}$$

Each basis function ϕ_j is continuous, thus ensuring a conforming approximation space: $S_0^h = \text{span}(\phi_1, \phi_2, \ldots, \phi_n) \subset \mathcal{H}^1_{E_0}$, where n is the number of nodes, as before. Note that there are precisely four basis functions that are nonzero on any particular tetrahedral element, corresponding to the four coefficients needed to define the linear approximation in the element. This also leads to a convenient implementation, exactly as in the triangular case.

Higher order tetrahedral elements are defined by introducing additional nodes. For example, the $\boldsymbol{P}_2$ element has additional mid-edge nodes as depicted in Figure 1.12. This gives ten nodes in each element, matching the ten coefficients needed to define a trivariate quadratic polynomial (of the form $a + bx + cy + dz + ex^2 + fy^2 + gz^2 + hxy + kxz + lyz$). On any triangular face (which defines a plane, $\hat{a}x + \hat{b}y + \hat{c}z = \hat{d}$), one of the variables, z say, can be eliminated in terms of a linear combination of $1, x$ and y, to give a bivariate

quadratic (in x, y) that is uniquely determined by its value at the six nodes of the $\boldsymbol{P}_2$ triangular element. As a result, continuity across inter-element faces, and hence a conforming approximation for (1.19), is assured.

More generally, $\boldsymbol{P}_m$ elements corresponding to continuous piecewise mth degree trivariate polynomial approximation are defined by an obvious generalization of the bivariate triangular analogue. All such tetrahedral elements have a gradient whose normal component is discontinuous across inter-element faces.

1.3.4 *Brick elements* ($\mathbb{R}^3$)

Three-dimensional approximation on cubes (or more generally *bricks*, which have six rectangular faces) is realized by taking the *tensor product* of lower dimensional elements. Thus the simplest conforming element for (1.19) is the trilinear $\boldsymbol{Q}_1$ element that takes the form $(ax + b)(cy + d)(ez + f)$ on each brick. Written as a linear combination, there are eight terms $1, x, y, z, xy, xz, yz, xyz$ and the eight coefficients are determined using the eight corner nodes, as illustrated in Figure 1.13. As a result, adopting the standard definition of a trilinear basis satisfying (1.28) there are precisely eight basis functions that are not identically zero within each element.

The recipe for higher order approximation on bricks is obvious. The $\boldsymbol{Q}_2$ triquadratic represented in Figure 1.13 has twenty-seven nodes; there are eight

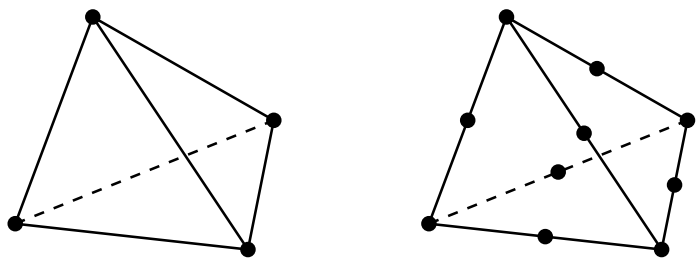

FIG. 1.12. Representation of $\boldsymbol{P}_1$ and $\boldsymbol{P}_2$ tetrahedral elements.

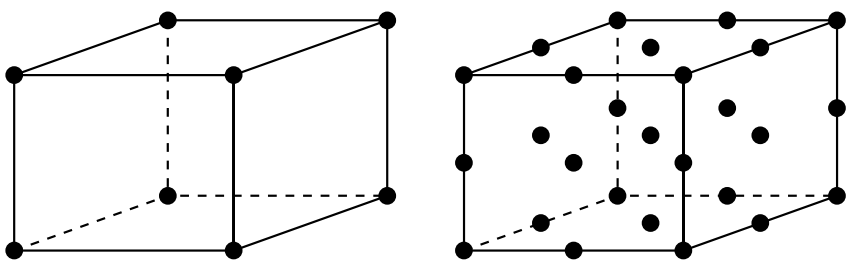

FIG. 1.13. Representation of $\boldsymbol{Q}_1$ and $\boldsymbol{Q}_2$ brick elements.

corner basis functions, twelve mid-edge basis functions, six mid-face basis functions and a single bubble function associated with the node at the centroid. Finally, we note that elements with six quadrilateral faces can be defined analogously to the two-dimensional case via a trilinear parametric mapping to the unit cube.

1.4 Implementation aspects

The computation of a finite element approximation consists of the following tasks. These are all built into the IFISS software.

(a) Input of the data on $\Omega, \partial\Omega_N, \partial\Omega_D$ defining the problem to be solved.
(b) Generation of a grid or mesh of elements.
(c) Construction of the Galerkin system.
(d) Solution of the discrete system, using a linear solver that exploits the sparsity of the finite element coefficient matrix.
(e) A posteriori error estimation.

In this section we focus on the core aspect (c) of setting up the discrete Galerkin system (1.21). Other key aspects, namely, the solution of this system and a posteriori error analysis, are treated in Chapter 2 and Section 1.5 respectively. Postprocessing of the solution is also required in general. This typically involves visualization and the calculation of derived quantities (e.g. boundary derivatives). A posteriori error analysis is particularly important. If the estimated errors are larger than desired, then the approximation space may be increased in dimension, either through local mesh subdivision (*h-refinement*), or by increasing the order of the local polynomial basis (*p-refinement*). An acceptable solution may then be calculated by cycling through steps (b)–(e) in an efficient way that builds on the existing structure, until the required error tolerance is satisfied.

The key idea in the implementation of finite element methodology is to consider everything "elementwise", that is, locally one element at a time. In effect the discrete problem is broken up; for example, (1.20) is rewritten as

$$\sum_{j=1}^{n} \mathbf{u}_j \int_{\Omega} \nabla\phi_j \cdot \nabla\phi_i = \sum_{j=1}^{n} \mathbf{u}_j \left\{ \sum_{\triangle_k \in \mathcal{T}_h} \int_{\triangle_k} \nabla\phi_j \cdot \nabla\phi_i \right\}. \tag{1.29}$$

Notice that when forming the sum over the elements in (1.29), we need only take account of those elements where the basis functions ϕ_i and ϕ_j are both nonzero. This means that entries a_{ij} and f_i in the Galerkin system (1.21) can be computed by calculating contributions from each of the elements, and then gathering (or *assembling*) them together.

If the kth element has n_k local degrees of freedom, then there are n_k basis functions that are not identically zero on the element. For example, in the case

of a mesh made up entirely of $\boldsymbol{P}_1$ triangles, we have $n_k = 3$ for all elements, so that in each $\triangle_k$ there are three *element* basis functions associated with the restriction of three different *global* basis functions ϕ_j. In the case of a mesh containing a mixture of $\boldsymbol{Q}_2$ rectangles and $\boldsymbol{P}_2$ triangles, we have $n_k = 9$ if element k is a rectangle and $n_k = 6$ otherwise. In all cases the local functions form an (element) basis set

$$\Xi_k := \{\psi_{k,1}, \psi_{k,2}, \ldots, \psi_{k,n_k}\}, \tag{1.30}$$

so that the solution within the element takes the form

$$u_h|_k = \sum_{i=1}^{n_k} \mathbf{u}_i^{(k)} \psi_{k,i}. \tag{1.31}$$

Using triangular elements, for example, and localizing (1.22) and (1.23), we need to compute a set of $n_k \times n_k$ element matrices A_k and a set of n_k-vectors $\mathbf{f}_k$ such that

$$A_k = [a_{ij}^{(k)}], \quad a_{ij}^{(k)} = \int_{\triangle_k} \nabla\psi_{k,i} \cdot \nabla\psi_{k,j}, \tag{1.32}$$

$$\mathbf{f}_k = [\boldsymbol{f}_i^{(k)}], \quad \boldsymbol{f}_i^{(k)} = \int_{\triangle_k} f\ \psi_{k,i} + \int_{\partial\Omega_N \cap \partial\triangle_k} g_N\ \psi_{k,i}. \tag{1.33}$$

The matrix A_k is referred to as the *element stiffness matrix* (*local stiffness matrix*) associated with element $\triangle_k$. Its construction for the cases of triangular and quadrilateral elements is addressed in Sections 1.4.1 and 1.4.2. (A completely analogous construction is required for $\mathbb{R}^3$, see Hughes [109, chap. 3].) Notice that for computational convenience the essential boundary condition has not been enforced in (1.33). This is the standard implementation; essential conditions are usually imposed after the assembly of the element contributions into the Galerkin matrix has been completed. We will return to this point in the discussion of the assembly process in Section 1.4.3.

1.4.1 *Triangular element matrices*

The first stage in the computation of the element stiffness matrix A_k is to map from a reference element $\triangle_*$ onto the given element $\triangle_k$, as illustrated in Figure 1.14. For straight sided triangles the local–global mapping is defined for all points $(x, y) \in \triangle_k$ and is given by

$$x(\xi, \eta) = x_1\chi_1(\xi, \eta) + x_2\chi_2(\xi, \eta) + x_3\chi_3(\xi, \eta) \tag{1.34}$$

$$y(\xi, \eta) = y_1\chi_1(\xi, \eta) + y_2\chi_2(\xi, \eta) + y_3\chi_3(\xi, \eta), \tag{1.35}$$

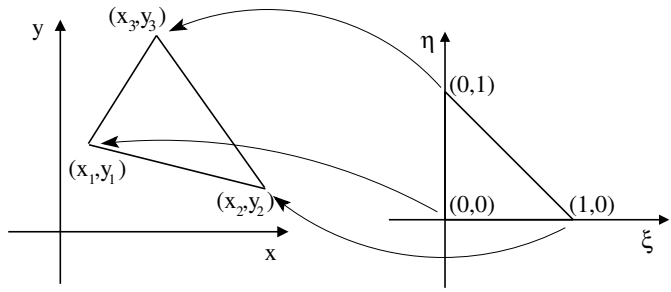

FIG. 1.14. Isoparametric mapping of $\boldsymbol{P}_1$ element.

where

$$\begin{aligned} \chi_1(\xi,\eta) &= 1-\xi-\eta \\ \chi_2(\xi,\eta) &= \xi \\ \chi_3(\xi,\eta) &= \eta \end{aligned} \tag{1.36}$$

are the $\boldsymbol{P}_1$ basis functions defined on the reference element. We note in passing that elements with curved sides can be generated using the analogous mapping defined by the $\boldsymbol{P}_2$ reference element basis functions illustrated in Figure 1.7.

Clearly, the map from the reference element onto $\triangle_k$ is (and has to be) differentiable. Thus, given a differentiable function $\varphi(\xi,\eta)$, we can transform derivatives via

$$\begin{bmatrix} \dfrac{\partial\varphi}{\partial\xi} \\ \dfrac{\partial\varphi}{\partial\eta} \end{bmatrix} = \begin{bmatrix} \dfrac{\partial x}{\partial\xi} & \dfrac{\partial y}{\partial\xi} \\ \dfrac{\partial x}{\partial\eta} & \dfrac{\partial y}{\partial\eta} \end{bmatrix} \begin{bmatrix} \dfrac{\partial\varphi}{\partial x} \\ \dfrac{\partial\varphi}{\partial y} \end{bmatrix}. \tag{1.37}$$

The *Jacobian matrix* in (1.37) may be simply calculated by substituting (1.36) into (1.34)–(1.35) and differentiating to give

$$J_k = \frac{\partial(x,y)}{\partial(\xi,\eta)} = \begin{bmatrix} x_2-x_1 & y_2-y_1 \\ x_3-x_1 & y_3-y_1 \end{bmatrix}. \tag{1.38}$$

Thus in this simple case, we see that J_k is a constant matrix over the reference element, and that the determinant

$$|J_k| = \begin{vmatrix} x_2-x_1 & y_2-y_1 \\ x_3-x_1 & y_3-y_1 \end{vmatrix} = \begin{vmatrix} 1 & x_1 & y_1 \\ 1 & x_2 & y_2 \\ 1 & x_3 & y_3 \end{vmatrix} = 2|\triangle_k| \tag{1.39}$$

is simply the ratio of the area of the mapped element $\triangle_k$ to that of the reference element $\triangle*$. The fact that $|J_k(\xi,\eta)| \neq 0$ for all points $(\xi,\eta) \in \triangle*$ is very important; it ensures that the inverse mapping from $\triangle_k$ onto the reference

element is uniquely defined and is differentiable. This means that the derivative transformation (1.37) can be inverted to give

$$\begin{bmatrix} \dfrac{\partial \varphi}{\partial x} \\ \dfrac{\partial \varphi}{\partial y} \end{bmatrix} = \begin{bmatrix} \dfrac{\partial \xi}{\partial x} & \dfrac{\partial \eta}{\partial x} \\ \dfrac{\partial \xi}{\partial y} & \dfrac{\partial \eta}{\partial y} \end{bmatrix} \begin{bmatrix} \dfrac{\partial \varphi}{\partial \xi} \\ \dfrac{\partial \varphi}{\partial \eta} \end{bmatrix}. \tag{1.40}$$

Thus we see that derivatives of functions defined on $\triangle_k$ satisfy

$$\begin{aligned} \frac{\partial \xi}{\partial x} &= \frac{1}{|J_k|}\frac{\partial y}{\partial \eta}, \qquad \frac{\partial \eta}{\partial x} = -\frac{1}{|J_k|}\frac{\partial y}{\partial \xi}, \\ \frac{\partial \xi}{\partial y} &= -\frac{1}{|J_k|}\frac{\partial x}{\partial \eta}, \quad \frac{\partial \eta}{\partial y} = \frac{1}{|J_k|}\frac{\partial x}{\partial \xi}. \end{aligned} \tag{1.41}$$

Given the basis functions on the master element $\psi_{*,i};\ i = 1, \ldots, n_k$, (see, e.g. Problem 1.3), the $\boldsymbol{P}_m$ element stiffness matrix A_k in (1.32) is easily computed:

$$\begin{aligned} a_{ij}^{(k)} &= \int_{\triangle_k} \frac{\partial \psi_{k,i}}{\partial x}\frac{\partial \psi_{k,j}}{\partial x} + \frac{\partial \psi_{k,i}}{\partial y}\frac{\partial \psi_{k,j}}{\partial y}\mathrm{d}x\,\mathrm{d}y \quad i,j = 1, \ldots, n_k \\ &= \int_{\triangle_*} \left\{ \frac{\partial \psi_{*,i}}{\partial x}\frac{\partial \psi_{*,j}}{\partial x} + \frac{\partial \psi_{*,i}}{\partial y}\frac{\partial \psi_{*,j}}{\partial y} \right\} |J_k|\,\mathrm{d}\xi\,\mathrm{d}\eta. \end{aligned} \tag{1.42}$$

In the specific case of the linear mapping given by (1.36), it is convenient to define the following coefficients:

$$\begin{aligned} b_1 &= y_2 - y_3; \quad b_2 = y_3 - y_1; \quad b_3 = y_1 - y_2; \\ c_1 &= x_3 - x_2; \quad c_2 = x_1 - x_3; \quad c_3 = x_2 - x_1; \end{aligned} \tag{1.43}$$

in which case (1.38)–(1.41) implies that

$$\begin{bmatrix} \dfrac{\partial \varphi}{\partial x} \\ \dfrac{\partial \varphi}{\partial y} \end{bmatrix} = \frac{1}{2|\triangle_k|} \begin{bmatrix} b_2 & b_3 \\ c_2 & c_3 \end{bmatrix} \begin{bmatrix} \dfrac{\partial \varphi}{\partial \xi} \\ \dfrac{\partial \varphi}{\partial \eta} \end{bmatrix}. \tag{1.44}$$

Combining (1.44) with (1.42) gives the general form of the stiffness matrix expressed in terms of the local derivatives of the element basis functions:

$$\begin{aligned} a_{ij}^{(k)} = &\int_{\triangle_*} \left(b_2\frac{\partial \psi_{*,i}}{\partial \xi} + b_3\frac{\partial \psi_{*,i}}{\partial \eta} \right) \left(b_2\frac{\partial \psi_{*,j}}{\partial \xi} + b_3\frac{\partial \psi_{*,j}}{\partial \eta} \right) \frac{1}{|J_k|}\mathrm{d}\xi\,\mathrm{d}\eta \\ &+ \int_{\triangle_*} \left(c_2\frac{\partial \psi_{*,i}}{\partial \xi} + c_3\frac{\partial \psi_{*,i}}{\partial \eta} \right) \left(c_2\frac{\partial \psi_{*,j}}{\partial \xi} + c_3\frac{\partial \psi_{*,j}}{\partial \eta} \right) \frac{1}{|J_k|}\mathrm{d}\xi\,\mathrm{d}\eta. \end{aligned} \tag{1.45}$$

With the simplest linear approximation, that is, $\psi_{*,i} = \chi_i$ (see (1.36)), the local derivatives $\partial\psi_{*,i}/\partial\xi$, $\partial\psi_{*,i}/\partial\eta$ are constant, so the local stiffness matrix is trivial to compute (see Problem 1.5).

From a practical perspective, the simplest way of effecting the local-global transformation given by (1.36) is to define local element functions using *triangular* or *barycentric* coordinates (see Problem 1.6).

1.4.2 *Quadrilateral element matrices*

In the case of quadrilateral elements (and rectangular elements in particular), the stiffness matrix A_k is typically computed by mapping as in Figure 1.10 from a reference element $\square_*$ onto the given element $\square_k$, and then using quadrature. For quadrilaterals the local–global mapping is defined for all points $(x, y) \in \square_k$ and is given by

$$x(\xi,\eta) = x_1\chi_1(\xi,\eta) + x_2\chi_2(\xi,\eta) + x_3\chi_3(\xi,\eta) + x_4\chi_4(\xi,\eta) \tag{1.46}$$

$$y(\xi,\eta) = y_1\chi_1(\xi,\eta) + y_2\chi_2(\xi,\eta) + y_3\chi_3(\xi,\eta) + y_4\chi_4(\xi,\eta), \tag{1.47}$$

where

$$\begin{aligned}
\chi_1(\xi,\eta) &= (\xi-1)(\eta-1)/4\\
\chi_2(\xi,\eta) &= -(\xi+1)(\eta-1)/4\\
\chi_3(\xi,\eta) &= (\xi+1)(\eta+1)/4\\
\chi_4(\xi,\eta) &= -(\xi-1)(\eta+1)/4
\end{aligned}$$

are the $\boldsymbol{Q}_1$ basis functions defined on the reference element (see Figure 1.10).

The map from the reference element onto $\square_k$ is differentiable, and derivatives are defined via (1.37), as in the triangular case. The big difference here is that the entries in the Jacobian matrix are *linear* functions of the coordinates (ξ, η) (cf. (1.38))

$$J_k = \frac{\partial(x,y)}{\partial(\xi,\eta)} = \begin{bmatrix} \sum_{j=1}^4 x_j \dfrac{\partial\chi_j}{\partial\xi} & \sum_{j=1}^4 y_j \dfrac{\partial\chi_j}{\partial\xi} \\ \sum_{j=1}^4 x_j \dfrac{\partial\chi_j}{\partial\eta} & \sum_{j=1}^4 y_j \dfrac{\partial\chi_j}{\partial\eta} \end{bmatrix}. \tag{1.48}$$

Note that the determinant $|J_k|$ is always a linear function of the coordinates, see Problem 1.7. In simple terms, the mapped element must have straight edges. If the mapped element $\square_k$ is a parallelogram then the Jacobian turns out to be a constant matrix.

A sufficient condition for a well-defined inverse mapping ($|J_k(\xi,\eta)| > 0$ for all points $(\xi, \eta) \in \square*$) is that the mapped element be convex. In this case, derivatives

on $\square_k$ can be computed[3] using (1.40), with

$$\begin{aligned} \frac{\partial \xi}{\partial x} &= \frac{1}{|J_k|}\sum_{j=1}^{4} y_j \frac{\partial \chi_j}{\partial \eta}, \qquad \frac{\partial \eta}{\partial x} = -\frac{1}{|J_k|}\sum_{j=1}^{4} y_j \frac{\partial \chi_j}{\partial \xi}, \\ \frac{\partial \xi}{\partial y} &= -\frac{1}{|J_k|}\sum_{j=1}^{4} x_j \frac{\partial \chi_j}{\partial \eta}, \quad \frac{\partial \eta}{\partial y} = \frac{1}{|J_k|}\sum_{j=1}^{4} x_j \frac{\partial \chi_j}{\partial \xi}, \end{aligned} \tag{1.49}$$

and the $\boldsymbol{Q}_m$ element stiffness matrix is computed via

$$a_{ij}^{(k)} = \int_{\square_*} \left\{ \frac{\partial \psi_{*,i}}{\partial x}\frac{\partial \psi_{*,j}}{\partial x} + \frac{\partial \psi_{*,i}}{\partial y}\frac{\partial \psi_{*,j}}{\partial y} \right\} |J_k| \, \mathrm{d}\xi \, \mathrm{d}\eta. \tag{1.50}$$

Note that if general quadrilateral elements are used then the integrals in (1.50) involve rational functions of polynomials.

Gauss quadrature is almost always used to evaluate the definite integrals that arise in the calculation of the element matrices A_k and the vectors $\mathbf{f}_k$. Quadrilateral elements are particularly amenable to quadrature because integration rules can be constructed by taking tensor products of the standard one-dimensional Gauss rules. This is the approach adopted in the IFISS software. The definite integral (1.50) is approximated by the summation

$$\bar{a}_{ij}^{(k)} = \sum_{s=1}^{m}\sum_{t=1}^{m} w_{st} |J_k(\xi_s,\eta_t)| \left\{ \frac{\partial \psi_{*,i}}{\partial x}\frac{\partial \psi_{*,j}}{\partial x} + \frac{\partial \psi_{*,i}}{\partial y}\frac{\partial \psi_{*,j}}{\partial y} \right\} \Bigg|_{(\xi_s,\eta_t)},$$

where the quadrature points (ξ_s, η_t) are those associated with one of the Gauss tensor-product hierarchy illustrated in Figure 1.15. The quadrature weights w_{st} are computed by taking the tensor product of the weights associated with the classical one-dimensional rule, see [109, pp. 141–145] for further details.

In one dimension, all polynomials of degree $2m-1$ can be integrated exactly using the classical m point Gauss rule. This is *optimal* in the sense that any

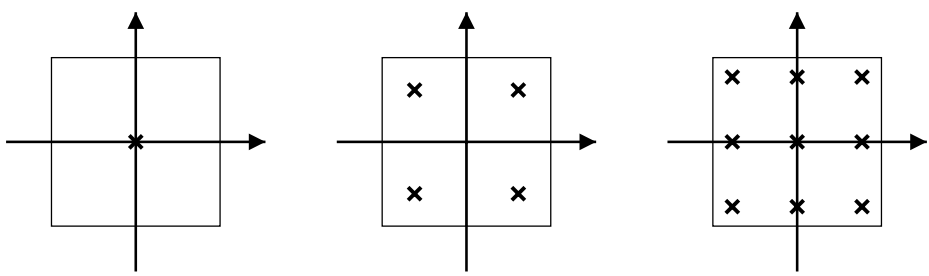

FIG. 1.15. Sampling points for 1×1, 2×2 and 3×3 Gauss quadrature rules.

[3]Using `deriv.m` and `qderiv.m` in IFISS.

rule with m points has precisely $2m$ free parameters (namely, the weights and positions of the quadrature points). Although the tensor-product rules are not optimal in this sense, the $m \times m$ rule does have the nice property that it exactly integrates all $\boldsymbol{Q}_{2m-1}$ functions. This means that in the case of grids of rectangular (or more generally parallelogram) elements, the bilinear element matrix A_k can be exactly computed using the 2×2 rule, see Problem 1.9. Similarly, the biquadratic element matrix A_k can be exactly integrated (for a rectangular element) if the 3×3 rule is used.

The element source vector (1.33) is also typically computed using quadrature. For example, the interior contribution to the source vector (1.33)

$$\boldsymbol{f}_i^{(k)} = \int_{\square *} f \psi_{*,i} \, |J_k| \mathrm{d}\xi \, \mathrm{d}\eta, \tag{1.51}$$

can be approximated via[4]

$$\bar{\boldsymbol{f}}_i^{(k)} = \sum_{s=1}^{m} \sum_{t=1}^{m} w_{st} f(\xi_s, \eta_t) \, \psi_{*,i}(\xi_s, \eta_t) \, |J_k(\xi_s, \eta_t)|. \tag{1.52}$$

The 2×2 rule would generally be used in the case of bilinear approximation, and the 3×3 rule if the approximation is biquadratic. Gauss integration rules designed for triangular elements are tabulated in [109, pp. 173–174].

1.4.3 *Assembly of the Galerkin system*

The assembly of the element contributions A_k and $\mathbf{f}_k$ into the Galerkin system is a reversal of the localization process illustrated in Figure 1.16.

The main computational issue is the need for careful bookkeeping to ensure that the element contributions are added into the correct locations in the coefficient matrix A and the vector $\mathbf{f}$. The simplest way of implementing the process is to represent the mapping between local and global entities using a connectivity matrix. For example, in the case of the mesh of $\boldsymbol{P}_1$ triangles illustrated in

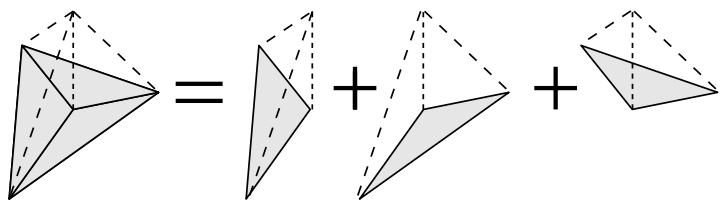

FIG. 1.16. Assembly of $\boldsymbol{P}_1$ global basis function from component element functions.

[4]Using `gauss_source.m` in IFISS.

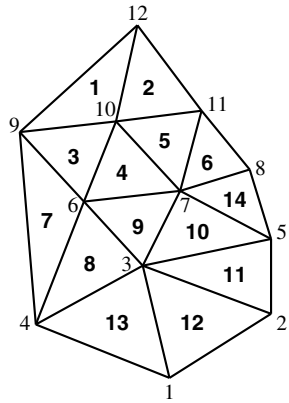

FIG. 1.17. Nodal and element numbering for the mesh in Figure 1.5.

Figure 1.17 we introduce the connectivity matrix defined by

$$\mathtt{P}^T = \begin{array}{c} \begin{array}{cccccccccccccc} \mathbf{1} & \mathbf{2} & \mathbf{3} & \mathbf{4} & \mathbf{5} & \mathbf{6} & \mathbf{7} & \mathbf{8} & \mathbf{9} & \mathbf{10} & \mathbf{11} & \mathbf{12} & \mathbf{13} & \mathbf{14} \end{array} \\ \left[\begin{array}{cccccccccccccc} 9 & 12 & 9 & 6 & 10 & 11 & 4 & 4 & 6 & 5 & 5 & 2 & 1 & 8 \\ 10 & 10 & 6 & 7 & 7 & 7 & 6 & 3 & 3 & 7 & 3 & 3 & 3 & 7 \\ 12 & 11 & 10 & 10 & 11 & 8 & 9 & 6 & 7 & 3 & 2 & 1 & 4 & 5 \end{array}\right], \end{array}$$

so that the index $\mathtt{j} = \mathtt{P}(\mathtt{k}, \mathtt{i})$ specifies the global node number of local node `i` in element `k`, and thus identifies the coefficient $\mathbf{u}_i^{(k)}$ in (1.31) with the global coefficient $\mathbf{u}_j$ in the expansion (1.18) of u_h. Given `P`, the matrices A_k and vectors $\mathbf{f}_k$ for the mesh in Figure 1.17 can be assembled into the Galerkin system matrix and vector using a set of nested loops.

```
k = 1:14
  j = 1:3
    i = 1:3
      Agal(P(k,i),P(k,j)) = Agal(P(k,i),P(k,j)) + A(k,i,j)
    endloop i
    fgal(P(k,j)) = fgal(P(k,j)) + f(k,j)
  endloop j
endloop k
```

A few observations are appropriate here. First, in a practical implementation, the Galerkin matrix `Agal` will be stored in an appropriate sparse format. Second, it should be apparent that as the elements are assembled in order above, then for any node s say, a stage will be reached when subsequent assemblies do not

affect node s (i.e. the sth row and column of the Galerkin matrix). When this stage is reached the variable is said to be fully summed; for example, variable 6 is fully summed after assembly of element **9**. This observation motivates the development of specialized direct solvers (known as *frontal solvers*) whereby the assembly process is intertwined with Gaussian elimination. In essence, as soon as a variable becomes fully summed, row operations can be performed to make entries below the diagonal zero and the modified row can then be saved for subsequent back-substitution, see for example Johnson [112, pp. 117–120].

It should also be emphasized that the intuitive element-by-element assembly embodied in the loop structure above is likely to be very inefficient; the inner loop involves indirect addressing and is too short to allow effective vectorization. The best way of generating efficient finite element code[5] is to work with blocks of elements and to reorder the loops so that the element loop `k` is the innermost. For real efficiency the number of elements in a block should be set so that all required data can fit into cache memory.

We now turn our attention to the imposition of essential boundary conditions on the assembled Galerkin system (1.21). We assume here that the basis functions are of Lagrangian type, that is, each basis function ϕ_j has a node $x_j \in \overline{\Omega}$ associated with it such that

$$\phi_j(x_j) = 1, \quad \phi_j(x_i) = 0 \qquad \text{for all nodes } x_i \neq x_j.$$

This property is depicted for the $\boldsymbol{P_2}$ basis functions in Figure 1.7. It follows from this assumption that for $x_j \in \partial\Omega_D$, $u_h(x_j) = \mathbf{u}_j$, where the required value of $\mathbf{u}_j$ is interpolated from the Dirichlet boundary data. See Ciarlet [44, Section 2.2] for treatment of more general basis functions.

Now consider how to impose this condition at node 5 of the mesh in Figure 1.17. Suppose that a preliminary version of the Galerkin matrix A is constructed via (1.22) for $1 \leq i, j \leq n + n_\partial$, and that in addition, all the contributions $\int_\Omega \phi_i f$ have been assembled into the right-hand side vector $\mathbf{f}$. There are then two things needed to specify the system (1.21) via (1.20) and (1.23): the given value of $\mathbf{u}_5$ must be included in the definition of the vector $\mathbf{f}$ of (1.23), and the fifth row and column of the preliminary Galerkin matrix must be deleted (since ϕ_5 is being removed from the space of test functions). The first step can be achieved by multiplying the fifth column of A by the specified boundary value $\mathbf{u}_5$ and then subtracting the result from $\mathbf{f}$. An alternative technique[6] is to retain the imposed degree of freedom in the Galerkin system by modifying the row and column (5, here) of the Galerkin matrix corresponding to the boundary node so that the diagonal value is unity and the off-diagonal entries are set to zero, and then setting the corresponding value of $\mathbf{f}$ to the boundary value $\mathbf{u}_5$. Notice that the modified Galerkin matrix thus has a multiple eigenvalue of unity, with multiplicity equal to the number of nodes on the Dirichlet part of the boundary.

[5]Embodied in the IFISS routines `femq1_diff.m` and `femq2_diff.m`.
[6]Embodied in the IFISS routine `nonzerobc.m`.

Finally we remark that it is easiest to treat any nonzero Neumann boundary conditions in the system (1.21) after the assembly process and the imposition of essential boundary conditions has been completed. At this stage, the boundary contribution in (1.23) can be assembled by running through the boundary edges on $\partial\Omega_N$ and evaluating the component edge contributions using standard (one-dimensional) Gauss quadrature.

1.5 Theory of errors

Our starting point is the generic problem (1.13)–(1.14). The associated weak formulation is the following: find $u \in \mathcal{H}^1_E$ such that

$$\int_\Omega \nabla u \cdot \nabla v = \int_\Omega v f + \int_{\partial\Omega} v\, g_N \quad \text{for all } v \in \mathcal{H}^1_{E_0}, \tag{1.53}$$

with spaces $\mathcal{H}^1_E$ and $\mathcal{H}^1_{E_0}$ given by (1.15) and (1.16), respectively.

To simplify the notation we follow the established convention of not distinguishing between scalar-valued functions (e.g. $u : \Omega \to \mathbb{R}$) and vector-valued functions (e.g. $\vec{u} : \Omega \to \mathbb{R}^d$) as long as there is no ambiguity. In general, a bold typeface is used to represent a space of vector-valued functions, and norms and inner products are to be interpreted componentwise.

Definition 1.1 ($\mathbf{L}_2(\Omega)$ inner product and norm). Let $L_2(\Omega)$ denote the space of square-integrable scalar-valued functions defined on Ω, see (1.11), with associated inner product $(\cdot,\cdot)$. The space $\mathbf{L}_2(\Omega)$ of square-integrable vector-valued functions defined on Ω consists of functions with each component in $L_2(\Omega)$, and has inner product

$$(\vec{u}, \vec{v}) := \int_\Omega \vec{u} \cdot \vec{v},$$

and norm

$$\|\vec{u}\| := (\vec{u}, \vec{u})^{1/2}.$$

For example, for two-dimensional vectors $\vec{u} = (u_x, u_y)$ and $\vec{v} = (v_x, v_y)$, $(\vec{u}, \vec{v}) = (u_x, v_x) + (u_y, v_y)$ and $\|\vec{u}\|^2 = \|u_x\|^2 + \|u_y\|^2$.

Our first task is to establish that a weak solution is uniquely defined. To this end, we assume two weak solutions satisfying (1.53); $u_1 \in \mathcal{H}^1_E$ and $u_2 \in \mathcal{H}^1_E$ say, and then try to establish that $u_1 = u_2$ everywhere. Subtracting the two variational equations shows that $u_1 - u_2 \in \mathcal{H}^1_{E_0}$ satisfies the equation

$$\int_\Omega \nabla(u_1 - u_2) \cdot \nabla v = 0 \quad \text{for all } v \in \mathcal{H}^1_{E_0}. \tag{1.54}$$

Substituting $v = u_1 - u_2$ then shows that $\|\nabla(u_1 - u_2)\| = 0$, and this implies that $u_1 - u_2$ is a constant function. To make progress the case of a pure Neumann

problem needs to be excluded. We can then use the additional fact that $u_1 = u_2$ on the Dirichlet part of the boundary. The following lemma holds the key to this.

Lemma 1.2 (Poincaré–Friedrichs inequality). *Assume that $\Omega \subset \mathbb{R}^2$ is contained in a square with side length L (and, in the case $\int_{\partial\Omega_N} \mathrm{ds} \neq 0$, that it has a sufficiently smooth boundary). Given that $\int_{\partial\Omega_D} \mathrm{ds} \neq 0$, it follows that*

$$\|v\| \leq L\,\|\nabla v\| \quad \textit{for all } v \in \mathcal{H}^1_{E_0}.$$

L is called the Poincaré constant.

This inequality is discussed in many texts on finite element error analysis; for example, [19, pp. 30–31], [28, pp. 128–130]. Establishing the inequality in the simplest case of a square domain Ω is a worthy exercise, see Problem 1.12. Making the choice $v = u_1 - u_2$ in Lemma 1.2 implies that the solution is unique.

Returning to (1.53), we identify the left-hand side with the bilinear form $a : \mathcal{H}^1(\Omega) \times \mathcal{H}^1(\Omega) \to \mathbb{R}$, and the right-hand side with the linear functional $\ell : \mathcal{H}^1(\Omega) \to \mathbb{R}$, so that

$$a(u,v) := (\nabla u, \nabla v); \qquad \ell(v) := (f,v) + (g_N, v)_{\partial\Omega_N}; \tag{1.55}$$

and restate the problem as:

Find $u \in \mathcal{H}^1_E$ such that

$$a(u,v) = \ell(v) \quad \text{for all } v \in \mathcal{H}^1_{E_0}. \tag{1.56}$$

The corresponding discrete problem (1.19) is then given by:

Find $u_h \in S^h_E$ such that

$$a(u_h, v_h) = \ell(v_h) \quad \text{for all } v_h \in S^h_0. \tag{1.57}$$

Assuming that the approximation is conforming, $S^h_E \subset \mathcal{H}^1_E$ and $S^h_0 \subset \mathcal{H}^1_{E_0}$, our task here is to estimate the quality of the approximation $u_h \approx u$.

We will outline the conventional (a priori) analysis of the approximation error arising using finite element approximation spaces in (1.57) in Section 1.5.1. Such error bounds are asymptotic in nature, and since they involve the true solution u they are not readily computable. We go on to discuss computable error bounds (usually referred to as a posteriori estimates) in Section 1.5.2.

1.5.1 *A priori error bounds*

To get a handle on the error, we can simply pick a generic $v \in \mathcal{H}^1_{E_0}$ and subtract $a(u_h, v)$ from (1.56) to give

$$a(u, v) - a(u_h, v) = \ell(v) - a(u_h, v).$$

This is the basic equation for the error: our assumption that $S^h_E \subset \mathcal{H}^1_E$ implies[7] that $e = u - u_h \in \mathcal{H}^1_{E_0}$ and satisfies

$$a(e, v) = \ell(v) - a(u_h, v) \quad \text{for all } v \in \mathcal{H}^1_{E_0}. \tag{1.58}$$

Note that $e \in \mathcal{H}^1_{E_0}$ since $S^h_E \subset \mathcal{H}^1_E$.

We now make explicit use of the fact that the underlying bilinear form $a(\cdot, \cdot)$ defines an inner product over the space $\mathcal{H}^1_{E_0} \times \mathcal{H}^1_{E_0}$, with an associated (*energy*) norm $\|\nabla u\| = a(u, u)^{1/2}$, see Problem 1.10. The starting point is the *Galerkin orthogonality property*: taking $v_h \in S^h_0$ in (1.58) and using (1.57) we have that

$$a(u - u_h, v_h) = 0 \quad \text{for all } v_h \in S^h_0. \tag{1.59}$$

In simple terms, the error $e \in \mathcal{H}^1_{E_0}$ is orthogonal to the subspace S^h_0, with respect to the energy inner product. An immediate consequence of (1.59) is the *best approximation property* established below.

Theorem 1.3. $\|\nabla u - \nabla u_h\| = \min\{\|\nabla u - \nabla v_h\| \colon v_h \in S^h_E\}$.

Proof Let $v_h \in S^h_E$, and note that $u - u_h \in \mathcal{H}^1_{E_0}$ so by definition

$$\begin{aligned}
\|\nabla(u - u_h)\|^2 &= a(u - u_h, u - u_h) \\
&= a(u - u_h, u - v_h + v_h - u_h) \\
&= a(u - u_h, u - v_h) + a(u - u_h, v_h - u_h) \\
&= a(u - u_h, u - v_h) \quad \text{(using Galerkin orthogonality)} \\
&\le \|\nabla(u - u_h)\| \, \|\nabla(u - v_h)\| \quad \text{(using Cauchy–Schwarz).}
\end{aligned}$$

Hence, for either $\|\nabla(u - u_h)\| = 0$ or $\|\nabla(u - u_h)\| \neq 0$, we have that

$$\|\nabla(u - u_h)\| \le \|\nabla(u - v_h)\| \quad \text{for all } v_h \in S^h_E. \tag{1.60}$$

Notice that the minimum is achieved since $u_h \in S^h_E$. □

The energy error bound (1.60) is appealingly simple, and moreover in the case $g_D = 0$ it leads to the useful characterization that

$$\|\nabla(u - u_h)\|^2 = \|\nabla u\|^2 - \|\nabla u_h\|^2, \tag{1.61}$$

[7] Recall that in practice, the essential boundary condition is interpolated, see (1.18), so that $u_h \neq g_D$ on $\partial\Omega_D$ whenever the boundary data g_D is not a polynomial. In such cases the error $u - u_h$ must be estimated using a more sophisticated *nonconforming* analysis, see Brenner & Scott [28, pp. 195ff] for details.

see Problem 1.11. (If u is known analytically, then (1.61) can be used to calculate the error in the energy norm without using elementwise integration.) The synergy between Galerkin orthogonality (1.59) and best approximation (1.60) is a reflection of the fact that u_h is the *projection* of u into the space S_E^h. This property will be exploited in Chapter 2, where fast solution algorithms are developed for the discrete problem (1.57).

The remaining challenge is to derive bounds on the error $u - u_h$ with respect to other norms, in particular, that associated with the *Hilbert space*[8] $\mathcal{H}^1(\Omega)$ introduced in Section 1.2. A formal definition is the following.

Definition 1.4 ($\mathcal{H}^1(\Omega)$ norm). Let $\mathcal{H}^1(\Omega)$ denote the set of functions u in $L_2(\Omega)$ possessing generalized[9] first derivatives. An inner product on $\mathcal{H}^1(\Omega)$ is given by

$$(u, v)_{1,\Omega} := (u, v) + (\nabla u, \nabla v), \tag{1.62}$$

and this induces the associated norm

$$\|u\|_{1,\Omega} := (\|u\|^2 + \|D^1 u\|^2)^{1/2} \tag{1.63}$$

where $D^1 u$ denotes the sum of squares of the first derivatives; for a two-dimensional domain Ω,

$$\|D^1 u\|^2 := \int_\Omega \left(\left(\frac{\partial u}{\partial x} \right)^2 + \left(\frac{\partial u}{\partial y} \right)^2 \right).$$

An important property of functions v in $\mathcal{H}^1(\Omega)$ is that they have a well-defined restriction to the boundary $\partial\Omega$. (This is an issue because functions in $\mathcal{H}^1(\Omega)$ need not be continuous.) The theoretical basis for this assertion is the following lemma.

Lemma 1.5 (Trace inequality). *Given a bounded domain Ω with a sufficiently smooth (e.g. polygonal) boundary $\partial\Omega$, a constant $C_{\partial\Omega}$ exists such that*

$$\|v\|_{\partial\Omega} \le C_{\partial\Omega} \|v\|_{1,\Omega} \quad \textit{for all } v \in \mathcal{H}^1(\Omega).$$

Notice that, in contrast, there is no constant C such that $\|v\|_{\partial\Omega} \le C \|v\|$ for every v in $L_2(\Omega)$, hence associating boundary values with $L_2(\Omega)$ functions is not meaningful. The proof of Lemma 1.5 is omitted, for details see Braess [19, pp. 48ff]. Applications of the trace inequality will be found in later sections.

Extending the energy error estimate of Theorem 1.3 to a general error bound in $\mathcal{H}^1(\Omega)$ is a simple consequence of the Poincaré–Friedrichs inequality.

[8]This means a vector space with an inner-product, which contains the limits of every Cauchy sequence that is defined with respect to the norm $\|\cdot\|_{1,\Omega}$.

[9]This includes functions like $|x|$ that are differentiable except at a finite number of points. To keep the exposition simple, we omit a formal definition; for details see [19, p. 28] or [28, pp. 24–27].

Proposition 1.6. *Let Ω satisfy the assumptions in Lemma* 1.2. *Then there is a constant C_Ω independent of v, such that*

$$\|\nabla v\| \leq \|v\|_{1,\Omega} \leq C_\Omega \|\nabla v\| \quad \text{for all } v \in \mathcal{H}^1_{E_0}. \tag{1.64}$$

Proof See Problem 1.13. □

We are now ready to state a *quasi-optimal* error bound that reflects the fact that $\|u - u_h\|_{1,\Omega}$ is proportional to the best possible approximation from the space S^h_E.

Theorem 1.7. *Let Ω satisfy the assumptions in Lemma* 1.2. *Then*

$$\|u - u_h\|_{1,\Omega} \leq C_\Omega \min_{v_h \in S^h_E} \|u - v_h\|_{1,\Omega}\,. \tag{1.65}$$

Proof Note that $u - v_h \in \mathcal{H}^1_{E_0}$ if $v_h \in S^h_E$. Combining (1.60) with (1.64) then gives (1.65). □

The best approximation error bound (1.60) is quite general in the sense that it is valid for any problem where the bilinear form $a(\cdot,\cdot)$ in (1.56) defines an inner product over the test space $\mathcal{H}^1_{E_0}$. The line of analysis above is not valid however, if the bilinear form $a(\cdot,\cdot)$ in the variational formulation is not symmetric, as, for example, for the convection–diffusion equation; see Chapter 3. In such cases, a priori error bounds in the underlying function space must be established using a different theoretical argument — typically using the coercivity and continuity of the underlying bilinear form over the space $\mathcal{H}^1_{E_0}$, see Problem 1.14. Further details are given in Chapter 3.

We now develop the general error bound (1.65) in the case of the finite element approximation spaces that were introduced in Sections 1.3.1 and 1.3.2. We first consider the simplest case of triangular elements using $\boldsymbol{P}_1$ (piecewise linear) approximation. That is, given a partitioning of the domain $\mathcal{T}_h$ consisting of triangular elements $\triangle_k$ we make the specific choice $S^h_0 = X^1_h$, where

$$X^1_h := \{v \in C^0(\Omega), v = 0 \text{ on } \partial\Omega_D;\ v|_\triangle \in \boldsymbol{P}_1,\ \forall \triangle \in \mathcal{T}_h\}. \tag{1.66}$$

We will state the error bound in the form of a theorem. We also need a couple of preliminary definitions.

Definition 1.8 ($\mathcal{H}^2(\Omega)$ norm). The set of functions $u \in \mathcal{H}^1(\Omega)$ that also possess generalized second derivatives can be identified with the Sobolev space $\mathcal{H}^2(\Omega)$. More precisely, $\mathcal{H}^2(\Omega) \subset \mathcal{H}^1(\Omega)$ is a Hilbert space that is complete with respect to the norm

$$\|u\|_{2,\Omega} := \left(\|u\|^2_{1,\Omega} + \left\|D^2 u\right\|^2\right)^{1/2},$$

where D^2u denotes the sum of squares of second derivatives. More specifically, in the case of a two-dimensional domain Ω

$$\left\|D^2u\right\|^2 := \int_\Omega \left(\left(\frac{\partial^2 u}{\partial x^2}\right)^2 + \left(\frac{\partial^2 u}{\partial x \partial y}\right)^2 + \left(\frac{\partial^2 u}{\partial y^2}\right)^2 \right).$$

Definition 1.9 ($\mathcal{H}^2$ regularity). The variational problem (1.56) is said to be *$\mathcal{H}^2$–regular* if there exists a constant C_Ω such that for every $f \in L_2(\Omega)$, there is a solution $u \in \mathcal{H}^1_E$ that is also in $\mathcal{H}^2(\Omega)$ such that

$$\|u\|_{2,\Omega} \leq C_\Omega \|f\| .$$

Theorem 1.10. *If the variational problem* (1.56) *is solved using a mesh of linear triangular elements, so that $S^h_0 = X^1_h$ in* (1.57)*, and if a minimal angle condition is satisfied* (*see* Definition 1.15)*, then there exists a constant $C_\mathbf{1}$ such that*

$$\|\nabla(u - u_h)\| \leq C_\mathbf{1}\, h \left\|D^2u\right\|, \tag{1.67}$$

where $\left\|D^2u\right\|$ measures the $\mathcal{H}^2$–regularity of the target solution, and h is the length of the longest triangle edge in the mesh.

Notice that if (1.56) is $\mathcal{H}^2$-regular, then (1.67) implies that the finite element solution u_h converges to the exact solution u in the limit $h \to 0$. The fact that the right-hand side of (1.67) is proportional to h is referred to as *first order* (or *linear*) convergence. Furthermore, Proposition 1.6 implies that if Lemma 1.2 is valid, then the order of convergence in $\mathcal{H}^1$ is the same as the order of convergence in the energy norm.

The issue of $\mathcal{H}^2$-regularity is central to the proof of Theorem 1.10, the first step of which is to break the bound (1.60) into pieces by introducing an appropriate interpolant $\pi_h u$ from the approximation space S^h_E. Making the specific choice $v_h = \pi_h u$ in (1.60) then gives

$$\|\nabla(u - u_h)\| \leq \|\nabla(u - \pi_h u)\| . \tag{1.68}$$

What is important here[10] is that $u \in \mathcal{H}^2(\Omega) \subset C^0(\Omega)$ so the simple piecewise linear interpolant $\pi_h u$, satisfying $\pi_h u(\mathbf{x}_i) = u(\mathbf{x}_i)$ at every vertex $\mathbf{x}_i$ of the triangulation, is a well-defined function in S^h_E (since $\pi_h u \in X^1_h$ in the case of zero boundary data). The localization of the error is now immediate since (1.68) can be broken up into elementwise error bounds

$$\|\nabla(u - \pi_h u)\|^2 = \sum_{\triangle_k \in \mathcal{T}_h} \|\nabla(u - \pi_h u)\|^2_{\triangle_k} . \tag{1.69}$$

[10]The relationship between continuous functions and Sobolev spaces is dependent on the domain Ω; if Ω is one-dimensional then $\mathcal{H}^1(\Omega) \subset C^0(\Omega)$, but for two-dimensional domains functions exist that are not bounded (hence not continuous) yet still have square integrable first derivatives, see [19, pp. 31–32].

The problem of estimating the overall error is now reduced to one of approximation theory — we need good estimates for the interpolation error on a typical element.

It is at this point that the local–global mapping in Section 1.4 plays an important role. Rather than estimating the error for every individual element, the idea is to map the element interpolation error from (1.69) onto the reference element, since the error can easily be bounded there in terms of derivatives of the interpolated function. This type of construction is referred to as a *scaling argument*. Each of the three stages in the process is summarized below in the form of a lemma. Note that h_k denotes the length of the longest edge of $\triangle_k$, and $\bar{u}$ denotes the mapped function defined on the reference element $\triangle *$.

Lemma 1.11. $\|\nabla(u - \pi_h u)\|^2_{\triangle_k} \leq 2\dfrac{h_k^2}{|\triangle_k|} \|\nabla(\bar{u} - \pi_h \bar{u})\|^2_{\triangle *}$.

Proof Define $e_k = (u - \pi_h u)|_{\triangle_k}$ and let $\bar{e}_k$ denote the mapped function defined on $\triangle *$. By definition

$$\begin{aligned} \|\nabla e_k\|^2_{\triangle_k} &= \int_{\triangle_k} \left(\frac{\partial e_k}{\partial x}\right)^2 + \left(\frac{\partial e_k}{\partial y}\right)^2 \mathrm{d}x\,\mathrm{d}y \\ &= \int_{\triangle *} \left(\left(\frac{\partial \bar{e}_k}{\partial x}\right)^2 + \left(\frac{\partial \bar{e}_k}{\partial y}\right)^2\right) 2|\triangle_k|\,\mathrm{d}\xi\mathrm{d}\eta, \end{aligned} \tag{1.70}$$

where the derivatives satisfy (1.44); in particular the first term is of the form

$$\left(\frac{\partial \bar{e}_k}{\partial x}\right)^2 = \frac{1}{4|\triangle_k|^2}\left(b_2 \frac{\partial \bar{e}_k}{\partial \xi} + b_3 \frac{\partial \bar{e}_k}{\partial \eta}\right)^2,$$

with b_2 and b_3 defined by (1.43). Using the facts that $(a+b)^2 \leq 2(a^2+b^2)$ and $|b_i| \leq h_k$, we get the bound

$$2|\triangle_k| \left(\frac{\partial \bar{e}_k}{\partial x}\right)^2 \leq \frac{h_k^2}{|\triangle_k|}\left(\left(\frac{\partial \bar{e}_k}{\partial \xi}\right)^2 + \left(\frac{\partial \bar{e}_k}{\partial \eta}\right)^2\right).$$

The second term in (1.70) can be bounded in exactly the same way ($|c_i| \leq h_k$). Summing the terms gives the stated result. □

The following bound is a special case of a general estimate for interpolation error in Sobolev spaces known as the *Bramble–Hilbert* lemma. In simple terms, the error due to linear interpolation in an unit triangle measured in the energy norm is bounded by the L^2 norm of the second derivative of the interpolation error.

Lemma 1.12.

$$\|\nabla(\bar{u} - \pi_h \bar{u})\|_{\triangle *} \leq C \left\|D^2(\bar{u} - \pi_h \bar{u})\right\|_{\triangle *} \equiv C \left\|D^2 \bar{u}\right\|_{\triangle *}. \tag{1.71}$$

Whilst proving the analogous result in $\mathbb{R}^1$ is a straightforward exercise, see Problem 1.15, the proof of (1.71) is technical and so is omitted. An accessible discussion can be found in [19, pp. 75–76], and a complete and rigorous treatment is given in [28, chap. 4].

Lemma 1.13. $\left\|D^2\bar{u}\right\|^2_{\triangle_*} \leq 18h_k^2 \dfrac{h_k^2}{|\triangle_k|} \left\|D^2u\right\|^2_{\triangle_k}$.

Proof By definition,

$$\begin{aligned}\left\|D^2\bar{u}\right\|^2_{\triangle_*} &= \int_{\triangle_*} \left(\frac{\partial^2\bar{u}}{\partial\xi^2}\right)^2 + \left(\frac{\partial^2\bar{u}}{\partial\xi\partial\eta}\right)^2 + \left(\frac{\partial^2\bar{u}}{\partial\eta^2}\right)^2 \mathrm{d}\xi\mathrm{d}\eta \\ &= \int_{\triangle_k} \left(\left(\frac{\partial^2 u}{\partial\xi^2}\right)^2 + \left(\frac{\partial^2 u}{\partial\xi\partial\eta}\right)^2 + \left(\frac{\partial^2 u}{\partial\eta^2}\right)^2\right) \frac{1}{2|\triangle_k|}\,\mathrm{d}x\,\mathrm{d}y, \qquad (1.72)\end{aligned}$$

where the derivatives are mapped using (1.37); in particular the first term is of the form

$$\begin{aligned}\left(\frac{\partial}{\partial\xi}\left(\frac{\partial u}{\partial\xi}\right)\right)^2 &= \left(c_3\frac{\partial}{\partial x}\left(\frac{\partial u}{\partial\xi}\right) - b_3\frac{\partial}{\partial y}\left(\frac{\partial u}{\partial\xi}\right)\right)^2 \\ &= \left(c_3^2\frac{\partial^2 u}{\partial x^2} - 2c_3b_3\frac{\partial^2 u}{\partial x\partial y} + b_3^2\frac{\partial^2 u}{\partial y^2}\right)^2 \\ &\leq 3\left(c_3^4\left(\frac{\partial^2 u}{\partial x^2}\right)^2 + 4c_3^2b_3^2\left(\frac{\partial^2 u}{\partial x\partial y}\right)^2 + b_3^4\left(\frac{\partial^2 u}{\partial y^2}\right)^2\right) \\ &\leq 12h_k^4\left(\left(\frac{\partial^2 u}{\partial x^2}\right)^2 + \left(\frac{\partial^2 u}{\partial x\partial y}\right)^2 + \left(\frac{\partial^2 u}{\partial y^2}\right)^2\right). \qquad (1.73)\end{aligned}$$

The second and third terms in (1.72) can be bounded in exactly the same way. Summing the three terms gives the stated result. □

The bound in Lemma 1.11 (and that in Lemma 1.13) involves the triangle aspect ratio $h_k^2/|\triangle_k|$. Keeping the aspect ratio small is equivalent to a minimum angle condition, as is shown in the following, see Figure 1.18.

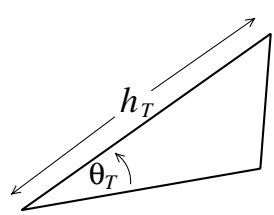

FIG. 1.18. Minimum angle condition.

Proposition 1.14. *Given any triangle, we have the equivalence relation*

$$\frac{h_T^2}{4}\sin\theta_T \le |\triangle_T| \le \frac{h_T^2}{2}\sin\theta_T, \tag{1.74}$$

where $0 < \theta_T \le \pi/3$ *is the smallest of the interior angles.*

Proof See Problem 1.16. □

The result (1.74) shows that bounding the aspect ratio is equivalent to ensuring that the minimum interior angle is bounded away from zero. Combining (1.74) with the bounds in Lemmas 1.11–1.13, we see that the interpolation error bound (1.69) satisfies

$$\|\nabla(u - \pi_h u)\|^2 \le C \sum_{\triangle_k \in \mathcal{T}_h} \frac{1}{\sin^2\theta_k} h_k^2 \left\|D^2 u\right\|_{\triangle_k}^2. \tag{1.75}$$

The bound (1.75) can be further simplified by making the assumption that the mesh refinement is shape regular as follows.

Definition 1.15 (Minimum angle condition). A sequence of triangular grids $\{\mathcal{T}_h\}$ is said to be *shape regular* if there exists a minimum angle $\theta_* \neq 0$ such that every element in $\mathcal{T}_h$ satisfies $\theta_T \ge \theta_*$.

In particular, shape regularity ensures that $1/\sin\theta_k \le 1/\sin\theta_*$ for all triangles in $\mathcal{T}_h$, so that (1.75) simplifies to

$$\|\nabla(u - \pi_h u)\|^2 \le C(\theta_*) \sum_{\triangle_k \in \mathcal{T}_h} h_k^2 \left\|D^2 u\right\|_{\triangle_k}^2. \tag{1.76}$$

Noting that $h_k \le h$ for all triangles $\triangle_k$ gives the desired uniform bound (i.e. independent of the triangulation)

$$\|\nabla(u - \pi_h u)\|^2 \le Ch^2 \sum_{\triangle_k \in \mathcal{T}_h} \left\|D^2 u\right\|_{\triangle_k}^2 = Ch^2 \left\|D^2 u\right\|^2.$$

Combining with (1.68) then gives the error bound (1.67) in Theorem 1.10. We also note that the less stringent *maximum angle condition*, which requires all angles to be uniformly bounded away from π, can also be used to obtain these results; see Krizek [126].

A similar argument can be used to establish a bound for the L_2 interpolation error associated with the function u itself. In particular, for a mesh of linear elements the following result can be readily established.

Proposition 1.16. $\|u - \pi_h u\|^2 \le C \sum_{\triangle_k \in \mathcal{T}_h} h_k^4 \left\|D^2 u\right\|_{\triangle_k}^2$.

Proof See Problem 1.17. □

Shape regularity is not required here, since derivatives are not mapped from $\triangle_k$ to the reference element.

We now consider the analogue of Theorem 1.10 in the case of grids of rectangular elements using $\boldsymbol{Q}_1$ approximation. (Recall from Problem 1.8 that the Jacobian reduces to a constant diagonal matrix in this case.) The analogues of Lemmas 1.11 and 1.13 are given below.

Proposition 1.17. *Given a rectangular element $\square_k$, with horizontal and vertical edges of lengths hx, hy, respectively, let π_h^1 be the standard bilinear interpolant, which agrees with the underlying function at the four vertices. Then*

$$\left\|\nabla(u-\pi_h^1 u)\right\|_{\square_k}^2 \leq \max\left\{\frac{hx}{hy},\frac{hy}{hx}\right\}\left\|\nabla(\bar{u}-\pi_h^1\bar{u})\right\|_{\square*}^2, \tag{1.77}$$

$$\left\|D^2\bar{u}\right\|_{\square*}^2 \leq h_k^2 \max\left\{\frac{hx}{hy},\frac{hy}{hx}\right\}\left\|D^2 u\right\|_{\square_k}^2, \tag{1.78}$$

where $h_k = \max\{hx, hy\}$.

Proof See Problem 1.18. □

Notice that the rectangle aspect ratio $\beta_T = \max\{hx/hy, hy/hx\}$ plays the same role as the triangle aspect ratio in Lemmas 1.11 and 1.13.

Definition 1.18 (Aspect ratio condition). A sequence of rectangular grids $\{\mathcal{T}_h\}$ is said to be *shape regular* if there exists a maximum rectangle edge ratio β_* such that every element in $\mathcal{T}_h$ satisfies $1 \leq \beta_T \leq \beta_*$.

A second key point is that the analogue of Lemma 1.12 also holds in this case,

$$\left\|\nabla(\bar{u}-\pi_h^1\bar{u})\right\|_{\square*} \leq C\left\|D^2(\bar{u}-\pi_h^1\bar{u})\right\|_{\square*} \equiv C\left\|D^2\bar{u}\right\|_{\square*}. \tag{1.79}$$

Combining the bounds (1.77), (1.79) and (1.78) gives the anticipated error estimate.

Theorem 1.19. *If the variational problem* (1.57) *is solved using a mesh of bilinear rectangular elements, and if the aspect ratio condition is satisfied (see* Definition 1.18*), then there exists a constant $C_{\mathbf{1}}$ such that*

$$\|\nabla(u-u_h)\| \leq C_{\mathbf{1}}\, h\, \left\|D^2 u\right\|, \tag{1.80}$$

where h is the length of the longest edge in $\mathcal{T}_h$.

Remark 1.20. If the degree of element distortion is small, a similar bound to (1.80) also holds in the case of $\boldsymbol{Q}_1$ approximation on grids of isoparametrically mapped quadrilateral elements. For grids of parallelograms, given an appropriate definition of shape regularity (involving a minimum angle and an aspect ratio condition) the convergence bound is identical to (1.80), see [19, Theorem 7.5].

The construction of the error estimate (1.80) via the intermediate results (1.77), (1.79) and (1.78) provides the basis for establishing error bounds when higher-order ($\boldsymbol{P}_m$, $\boldsymbol{Q}_m$, with $m \geq 2$) approximation spaces are used.

Theorem 1.21. *Using a higher-order finite element approximation space $\boldsymbol{P}_m$ or $\boldsymbol{Q}_m$ with $m \geq 2$ leads to the higher-order convergence bound*

$$\|\nabla(u - u_h)\| \leq C_{\mathbf{m}}\, h^m \left\|D^{m+1}u\right\|. \tag{1.81}$$

In other words, we get mth order convergence as long as the regularity of the target solution is good enough. Note that $\left\|D^{m+1}u\right\| < \infty$ if and only if the (m+1)st generalized derivatives of u are in $L_2(\Omega)$.

For example, using biquadratic approximation on a square element grid, we have the following analogue of Proposition 1.17.

Proposition 1.22. *For a grid of square elements $\square_k$ with edges of length h, let π_h^2 be the standard biquadratic interpolant, which agrees with the underlying function at nine points, see Figure 1.11. Then*

$$\left\|\nabla(u - \pi_h^2 u)\right\|_{\square_k}^2 \leq \left\|\nabla(\bar{u} - \pi_h^2 \bar{u})\right\|_{\square_*}^2, \tag{1.82}$$

$$\left\|D^3 \bar{u}\right\|_{\square_*}^2 \leq h^4 \left\|D^3 u\right\|_{\square_k}^2. \tag{1.83}$$

Proof See Problem 1.19. □

Combining (1.82) and (1.83) with the reference element bound given by the Bramble–Hilbert lemma (in this case bounding in terms of the third derivatives; cf. Lemma 1.12)

$$\left\|\nabla(\bar{u} - \pi_h^2 \bar{u})\right\|_{\square_*} \leq C \left\|D^3(\bar{u} - \pi_h^2 \bar{u})\right\|_{\square_*} \equiv C \left\|D^3 \bar{u}\right\|_{\square_*} \tag{1.84}$$

leads to (1.81) with $m = 2$.

To conclude this section, we will use the problems in Examples 1.1.3 and 1.1.4 to illustrate that the orders of convergence suggested by the error bounds (1.80) and (1.81) are typical of the behavior of the error as the grid is successively refined. An assessment of the orders of convergence that is obtained for the problems in Examples 1.1.1 and 1.1.2 are given as Computational Exercises 1.1 and 1.2 respectively. Results for the problem in Example 1.1.3 are given in Table 1.1. The error measure E_h used here is the difference between the exact and the discrete energy, that is

$$E_h = \left| \|\nabla u\|^2 - \|\nabla u_h\|^2 \right|^{1/2}. \tag{1.85}$$

If zero essential boundary conditions are imposed, then $\|\nabla u\| \geq \|\nabla u_h\|$ and E_h is identical to the energy error $\|\nabla(u - u_h)\|$, see Problem 1.11. Notice how the $\boldsymbol{Q}_1$ errors in Table 1.1 decrease by a factor of two for every successive refinement,[11] whereas the $\boldsymbol{Q}_2$ errors ultimately decrease by a factor of four. The outcome is that biquadratic elements are more accurate than bilinear elements — in fact they

[11] ℓ is the *grid parameter* specification in the IFISS software that is associated with the tabulated entry.

Table 1.1 *Energy error E_h for Example 1.1.3: ℓ is the grid refinement level; h is $2^{1-\ell}$ for $\boldsymbol{Q}_1$ approximation, and $2^{2-\ell}$ for $\boldsymbol{Q}_2$ approximation.*

ℓ	$\boldsymbol{Q}_1$	$\boldsymbol{Q}_2$	n
2	5.102×10^{-2}	6.537×10^{-3}	9
3	2.569×10^{-2}	2.368×10^{-3}	49
4	1.287×10^{-2}	5.859×10^{-4}	225
5	6.437×10^{-3}	1.460×10^{-4}	961
6	3.219×10^{-3}	3.646×10^{-5}	3969

Table 1.2 *Energy error E_h for Example 1.1.4.*

ℓ	$\boldsymbol{Q}_1$	$\boldsymbol{Q}_2$	n
2	1.478×10^{-1}	9.860×10^{-2}	33
3	9.162×10^{-2}	6.207×10^{-2}	161
4	5.714×10^{-2}	3.909×10^{-2}	705
5	3.577×10^{-2}	2.462×10^{-2}	2945

are generally more cost-effective wherever the underlying solution is sufficiently smooth if reasonable accuracy is required. For example, the $\boldsymbol{Q}_2$ solution on the coarsest grid has approximately $1/4^3$ of the degrees of freedom of the $\boldsymbol{Q}_1$ solution on the second finest grid, yet both are of comparable accuracy.

If the weak solution is not smooth, then the superiority of the $\boldsymbol{Q}_2$ approximation method over the simpler $\boldsymbol{Q}_1$ method is not so clear. To illustrate this, the energy differences E_h computed in the case of the singular problem in Example 1.1.4 are tabulated in Table 1.2. Notice that — in contrast to the behavior in Table 1.1 — the $\boldsymbol{Q}_1$ and $\boldsymbol{Q}_2$ errors both decrease by a factor of approximately $2^{2/3} \approx 1.5874$ with every successive refinement of the grid. The explanation for this is that the solution regularity is between $\mathcal{H}^1$ and $\mathcal{H}^2$ in this case,[12] see Problem 1.20. The upshot is that in place of (1.80) and (1.81), the following convergence bound is the best that can be achieved (for all $\varepsilon > 0$):

$$\|\nabla(u - u_h)\| \leq C_{\mathbf{m}}(\epsilon)\, h^{2/3-\varepsilon} \tag{1.86}$$

using approximation of arbitrary order $m \geq 1$!

When solving problems like those in Examples 1.1.3 and 1.1.4, it is natural to try to design rectangular or triangular meshes that concentrate the degrees

[12] Introducing Sobolev spaces with fractional indices as in Johnson [112, pp. 92–94], it may be shown that $u \in \mathcal{H}^{5/3-\varepsilon}$.

Table 1.3 *Energy error E_h for stretched grid solutions of Example 1.1.4: $\ell = 4$.*

α	$\boldsymbol{Q}_1$	$\boldsymbol{Q}_2$
1	9.162×10^{-2}	6.207×10^{-2}
5/4	6.614×10^{-2}	3.723×10^{-2}
3/2	7.046×10^{-2}	2.460×10^{-2}
2	1.032×10^{-1}	2.819×10^{-2}

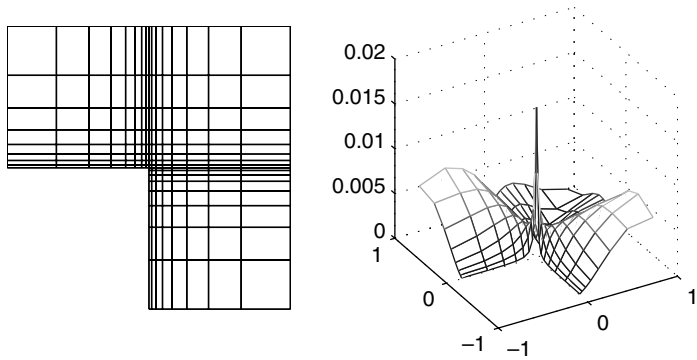

FIG. 1.19. Stretched level 4 grid with $\alpha = 3/2$ (left) for Example 1.1.4 and surface plot (right) of the estimated error using $\boldsymbol{Q}_1$ approximation (see Section 1.5.2).

of freedom in the neighborhood of the singularity. The motivation for doing this is the intermediate bound (1.76), which suggests that it is important to try to balance the size of h_k with that of $\|D^2 u\|_{\triangle_k}$. Roughly speaking, h_k should be small in those elements where the derivatives of u are large. To illustrate the idea, Table 1.3 lists the errors E_h obtained when solving the problem in Example 1.1.4 using tensor-product grids that are geometrically stretched towards the singularity, with successive element edges a factor α times longer than the adjacent edge, see Figure 1.19. Notice that comparing the results in Table 1.3 with those in Table 1.2, we see that an appropriately stretched grid of $\boldsymbol{Q}_2$ elements with 161 degrees of freedom, gives better accuracy than that obtained using a uniform grid with 2945 degrees of freedom — the challenge here is to determine the optimal stretching a priori!

1.5.2 *A posteriori error bounds*

The fact that physically interesting problems typically have singularities is what motivates the concept of a posteriori error estimation. Specifically, given a finite element subdivision $\mathcal{T}_h$ and a solution u_h, we want to compute a local

(element) error estimator η_T such that $\|\nabla\eta_T\|$ approximates the local energy error $\|\nabla(u-u_h)\|_T$ for every element T in $\mathcal{T}_h$. An important factor is the requirement that η_T should be cheap to compute — as a rule of thumb, the computational work should scale linearly as the number of elements is increased — yet there should be guaranteed accuracy in the sense that the estimated global error should give an upper bound on the exact error, so that

$$\|\nabla(u-u_h)\|^2 \equiv \sum_{T\in\mathcal{T}_h} \|\nabla(u-u_h)\|_T^2 \leq C(\theta_*) \sum_{T\in\mathcal{T}_h} \eta_T^2 \tag{1.87}$$

with a constant C that depends only on shape regularity. If, in addition to satisfying (1.87), η_T provides a lower bound for the exact local error

$$\eta_T \leq C(\theta_{\omega_T}) \|\nabla(u-u_h)\|_{\omega_T}, \tag{1.88}$$

where ω_T typically represents a local patch of elements adjoining T, then the estimator η_T is likely to be effective if it is used to drive an adaptive refinement process. For the problem in Example 1.1.4, such a process will give rise to successive meshes that are selectively refined in the vicinity of the singularity so as to equidistribute the error among all elements and enhance overall cost effectiveness.

The two key aspects of error estimation are *localization* and *approximation*. The particular strategy that is built into the IFISS software is now described. The starting point is the characterization (1.58) of the error $e = u - u_h \in \mathcal{H}^1_{E_0}$:

$$a(e,v) = \ell(v) - a(u_h,v) \quad \text{for all } v \in \mathcal{H}^1_{E_0}. \tag{1.89}$$

For simplicity, it is assumed here that Neumann data is homogeneous, so that $\ell(v) = (f,v)$. Using the shorthand notation $(u,v)_T := \int_T uv$ and $a(u,v)_T := \int_T \nabla u\cdot\nabla v$ to represent the localized L_2 and energy inner products respectively, the error equation (1.89) may be broken up into element contributions

$$\sum_{T\in\mathcal{T}_h} a(e,v)_T = \sum_{T\in\mathcal{T}_h} (f,v)_T - \sum_{T\in\mathcal{T}_h} a(u_h,v)_T. \tag{1.90}$$

Integrating by parts elementwise then gives

$$-a(u_h,v)_T = (\nabla^2 u_h, v)_T - \sum_{E\in\mathcal{E}(T)} \langle \nabla u_h\cdot\vec{n}_{E,T}, v\rangle_E, \tag{1.91}$$

where $\mathcal{E}(T)$ denotes the set of edges (faces in $\mathbb{R}^3$) of element T, $\vec{n}_{E,T}$ is the outward normal with respect to E, $\langle\cdot,\cdot\rangle_E$ is the L_2 inner product on E, and $\nabla u_h\cdot\vec{n}_{E,T}$ is the discrete (outward-pointing) normal flux. The finite element approximation typically has a discontinuous normal derivative across inter-element boundaries. Consequently it is convenient to define the *flux jump* across edge or face E adjoining elements T and S as

$$\left[\!\left[\frac{\partial v}{\partial n}\right]\!\right] := (\nabla v|_T - \nabla v|_S)\cdot\vec{n}_{E,T} = (\nabla v|_S - \nabla v|_T)\cdot\vec{n}_{E,S}, \tag{1.92}$$

and then to *equidistribute* the flux jump contribution in (1.90) to the adjoining elements in equal proportion (with an appropriate modification for elements that have one or more edges/faces adjoining $\partial\Omega$):

$$\sum_{T\in\mathcal{T}_h} a(e,v)_T = \sum_{T\in\mathcal{T}_h} \left[(f+\nabla^2 u_h, v)_T - \frac{1}{2}\sum_{E\in\mathcal{E}(T)} \left\langle \left[\!\left[\frac{\partial u_h}{\partial n} \right]\!\right], v \right\rangle_E \right]. \tag{1.93}$$

It is evident from the structure of the right-hand side of equation (1.93) that e has two distinct components; these are the (element) *interior residual* $R_T := \{f+\nabla^2 u_h\}|_T$, and the (inter-element) flux jump $R_E := [\![\partial u_h/\partial n]\!]$. Notice also that if u_h agrees with the classical solution everywhere then both R_T and R_E are identically zero. The residual terms R_T and R_E enter either implicitly or explicitly into the definition of many finite element error estimators.

In the remainder of this section we concentrate on the specific case of S_0^h being defined by the $\boldsymbol{P}_1$ or $\boldsymbol{Q}_1$ approximation over a triangular or rectangular element subdivision. The appeal of these lowest order methods is their simplicity; the flux jump is piecewise constant in the $\boldsymbol{P}_1$ case, and in both cases the interior residual $R_T = f|_T$ is independent of u_h and thus can be computed a priori. As a further simplification, R_T can be approximated by a constant R_T^0 by projecting f onto the space of piecewise constant functions.

To define a consistent flux jump operator with respect to elements adjoining $\partial\Omega$, some additional notation is needed. We let $\mathcal{E}_h = \cup_{T\in\mathcal{T}_h}\mathcal{E}(T)$ denote the set of all edges split into interior and boundary edges via

$$\mathcal{E}_h := \mathcal{E}_{h,\Omega} \cup \mathcal{E}_{h,D} \cup \mathcal{E}_{h,N};$$

where $\mathcal{E}_{h,\Omega} := \{E\in\mathcal{E}_h : E\subset\Omega\}$, $\mathcal{E}_{h,D} := \{E\in\mathcal{E}_h : E\subset\partial\Omega_D\}$ and $\mathcal{E}_{h,N} := \{E\in\mathcal{E}_h : E\subset\partial\Omega_N\}$. We then define the operator

$$R_E^* = \begin{cases} \frac{1}{2}[\![\partial u_h/\partial n]\!] & E\in\mathcal{E}_{h,\Omega} \\ -\nabla u_h\cdot\vec{n}_{E,T} & E\in\mathcal{E}_{h,N} \\ 0 & E\in\mathcal{E}_{h,D}. \end{cases}$$

The fact that the exact error e is characterized by the enforcement of (1.93) over the space $\mathcal{H}^1_{E_0}$ provides us with a handle for estimating the local error in each element T. Specifically, if a suitable (finite-dimensional) approximation space, $\mathcal{Q}_T$ say, is constructed, then an approximation to $e\,|_T$ can be obtained by enforcing (1.93) elementwise. Specifically, a function $e_T\in\mathcal{Q}_T$ is computed such that

$$(\nabla e_T, \nabla v)_T = (R_T^0, v)_T - \sum_{E\in\mathcal{E}(T)} \langle R_E^*, v\rangle_E, \tag{1.94}$$

for all $v\in\mathcal{Q}_T$, and the local error estimator is the energy norm of e_T

$$\eta_T = \|\nabla e_T\|_T. \tag{1.95}$$

Making an appropriate choice of approximation space $\mathcal{Q}_T$ in (1.94) is clearly crucial. A clever choice (due to Bank & Weiser [9]) is the "correction" space

$$\mathcal{Q}_T = Q_T \oplus B_T \tag{1.96}$$

consisting of edge and interior bubble functions, respectively;

$$Q_T = \text{ span } \{\psi_E : E \in \mathcal{E}(T) \cap (\mathcal{E}_{h,\Omega} \cup \mathcal{E}_{h,N})\} \tag{1.97}$$

where $\psi_E : T \to \mathbb{R}$ is the quadratic (or biquadratic) edge-bubble that is zero on the other two (or three) edges of T. B_T is the space spanned by interior cubic (or biquadratic) bubbles ϕ_T such that $0 \le \phi_T \le 1$, $\phi_T = 0$ on ∂T and $\phi_T = 1$ only at the centroid. The upshot is that for each triangular (or rectangular) element a 4×4 (or 5×5) system of equations must be solved to compute e_T.[13]

A feature of the choice of space (1.97) is that $(\nabla v, \nabla v)_T > 0$ for all functions v in $\mathcal{Q}_T$ (intuitively, a constant function in T cannot be represented as a linear combination of bubble functions), so the local problem (1.94) is well posed. This means that the element matrix systems are all non-singular, see Problem 1.21. This is important for a typical element T that has no boundary edges, since the local problem (1.94) represents a weak formulation of the Neumann problem:

$$-\nabla^2 e_T = f \quad \text{in } T \tag{1.98}$$

$$\frac{\partial e_T}{\partial n} = -\frac{1}{2}\left[\!\left[\frac{\partial u_h}{\partial n}\right]\!\right] \quad \text{on } E \in \mathcal{E}(T), \tag{1.99}$$

suggesting that a compatibility condition cf. (1.4)

$$\int_T f - \frac{1}{2}\sum_{E\in\mathcal{E}(T)} \int_E \left[\!\left[\frac{\partial u_h}{\partial n}\right]\!\right] = 0, \tag{1.100}$$

needs to be satisfied in order to ensure the existence of e_T. The difficulty associated with the need to enforce (1.100) is conveniently circumvented by the choice (1.97).

To illustrate the effectiveness of this very simple error estimation procedure, the analytic test problem in Example 1.1.3 is discretized using uniform grids of $\boldsymbol{Q}_1$ elements, and a comparison between the exact energy error $\|\nabla e\|$ and the estimated global error $\eta = \left(\sum_{T\in\mathcal{T}_h} \eta_T^2\right)^{1/2}$ is given in Table 1.4. The close agreement between the estimated and exact errors is quite amazing.[14] Another virtue of the estimator illustrated by Table 1.4 is the fact that the *global effectivity index* $X_\eta := \eta / \|\nabla e\|$ converges to unity as $h \to 0$. This property is usually referred to as *asymptotic exactness*.

The results in Table 1.4 suggest that the estimator η_T satisfies the required error bound (1.87) (with a proportionality constant $C(\theta_*)$ that is close to unity if

[13] This is embodied in the IFISS routine `diffpost_p.m`.

[14] Although performance deteriorates using stretched meshes, the agreement between exact and estimated errors is quite acceptable, see Computational Exercise 1.3.

Table 1.4 *Comparison of estimated and exact errors for Example 1.1.3.*

ℓ	$\|\nabla(u-u_h)\|$	η	X_η
2	5.032×10^{-2}	4.954×10^{-2}	0.9845
3	2.516×10^{-2}	2.511×10^{-2}	0.9980
4	1.258×10^{-2}	1.257×10^{-2}	0.9992
5	6.291×10^{-3}	6.288×10^{-3}	0.9995

the elements are not too distorted). A precise result is stated below. This should also be compared with the a priori error bound given in Theorem 1.19.

Theorem 1.23. *If the variational problem* (1.57) *is solved using a mesh of bilinear rectangular elements, and if the rectangle aspect ratio condition is satisfied with β_* given in Definition* 1.18*, then the estimator $\eta_T \equiv \|\nabla e_T\|_T$ computed via* (1.94) *using the approximation space* (1.97) *gives the bound*

$$\|\nabla(u-u_h)\| \le C(\beta_*)\left(\sum_{T\in\mathcal{T}_h}\eta_T^2 + h^2\sum_{T\in\mathcal{T}_h}\left\|R_T - R_T^0\right\|_T^2\right)^{1/2}, \tag{1.101}$$

where h is the length of the longest edge in $\mathcal{T}_h$.

Remark 1.24. If f is a piecewise constant function then the consistency error term $\left\|R_T - R_T^0\right\|_T$ is identically zero. Otherwise, if f is smooth, this term represents a high-order perturbation. In any case the estimator η_T is reliable; for further details see Verfürth [205].

A proof of Theorem 1.23 is outlined below. An important difference between the a priori bound (1.80) and the a posteriori bound (1.101) is that $\mathcal{H}^2$-regularity is not assumed in the latter case. This adds generality (since the bound (1.101) applies even if the problem is singular) but raises the technical issue within the proof of Theorem 1.23 of having to approximate a possibly discontinuous $\mathcal{H}^1$ function. Since point values of $\mathcal{H}^1(\Omega)$ functions are not defined for $\Omega \subset \mathbb{R}^2$, an alternative to interpolation using local averaging over neighborhoods of the vertices of the subdivision is required. This leads to the quasi-interpolation estimates (due to Clément [45]) given in the following lemma. For a detailed discussion, see Brenner & Scott [28, pp. 118–120].

Lemma 1.25. *Given $e \in \mathcal{H}^1_{E_0}$ there exists a quasi-interpolant $e_h^* \in S_0^h$ such that,*

$$\|e - e_h^*\|_T \le C_1(\beta_{\tilde\omega_T})\, h_T\, \|\nabla e\|_{\tilde\omega_T} \quad \textit{for all } T \in \mathcal{T}_h, \tag{1.102}$$

$$\|e - e_h^*\|_E \le C_2(\beta_{\tilde\omega_T})\, h_E^{1/2}\, \|\nabla e\|_{\tilde\omega_T} \quad \textit{for all } E \in \mathcal{E}_h, \tag{1.103}$$

where $\tilde{\omega}_T$ is the patch of all the neighboring elements that have at least one vertex connected to a vertex of element T.

Notice that the constants in (1.102) and (1.103) depend only on the maximum aspect ratio over all elements in the patch. The proof of Theorem 1.23 will also require so-called *local inverse estimates*. A typical example is given in the lemma below. A proof for low-order basis functions is provided; see [28, Section 4.5], [44, Section 3.2] for more general analysis.

Lemma 1.26. *Given a polynomial function u_k defined in a triangular or rectangular element T, a constant C exists, depending only on the element aspect ratio, such that*

$$\|\nabla u_k\|_T \leq C h_T^{-1} \|u_k\|_T \,, \tag{1.104}$$

where h_T is the length of the longest edge of T.

Proof This is a standard scaling argument of the type used in the proof of Lemma 1.11. In the case of triangular elements with $\boldsymbol{P}_1$ (linear) basis functions, the argument of that proof gives

$$\|\nabla u_k\|^2_{\triangle_k} \leq 2\frac{h_k^2}{|\triangle_k|} \|\nabla \bar{u}_k\|^2_{\triangle_*} . \tag{1.105}$$

Note that

$$\bar{u}_k \mapsto \|\nabla \bar{u}_k\|_{\triangle_*} , \quad \bar{u}_k \mapsto \|\bar{u}_k\|_{\triangle_*}$$

constitute a seminorm and norm, respectively, on finite-dimensional spaces. It follows that, as in the equivalence of norms on finite-dimensional spaces,

$$\|\nabla \bar{u}_k\|_{\triangle_*} \leq C \|\bar{u}_k\|_{\triangle_*} . \tag{1.106}$$

Mapping back to the original element, we have

$$\|\bar{u}_k\|^2_{\triangle_*} = \frac{1}{2|\triangle_k|} \|u_k\|^2_{\triangle_k} , \tag{1.107}$$

and combining (1.105), (1.106), (1.107) with (1.74) gives the stated result. The proof for a rectangular element is left as an exercise, see Problem 1.22. □

Returning to the proof of Theorem 1.23, the first step is to use Galerkin orthogonality (1.59), the error equation (1.89) and the definition of R_E^*:

$$\begin{aligned}
\|\nabla e\|^2 &= a(e,e) \\
&= a(e, e-e_h^*) \quad (\text{setting } v_h = e_h^* \text{ in (1.59)}) \\
&= \ell(e-e_h^*) - a(u_h, e-e_h^*) \quad (\text{setting } v = e-e_h^* \text{ in (1.89)}) \\
&= \sum_{T\in\mathcal{T}_h} \left\{ (R_T, e-e_h^*)_T - \sum_{E\in\mathcal{E}(T)} \langle R_E^*, e-e_h^*\rangle_E \right\} \quad (\text{using (1.91)}) \\
&\le C(\beta_*) \sum_{T\in\mathcal{T}_h} \left\{ h_T \|R_T\|_T \|\nabla e\|_{\tilde\omega_T} + \sum_{E\in\mathcal{E}(T)} h_E^{1/2} \|R_E^*\|_E \|\nabla e\|_{\tilde\omega_T} \right\} \\
&\le C(\beta_*) \left(\sum_{T\in\mathcal{T}_h} \|\nabla e\|_{\tilde\omega_T}^2 \right)^{1/2} \left(\sum_{T\in\mathcal{T}_h} \left\{ h_T \|R_T\|_T + \sum_E h_E^{1/2} \|R_E^*\|_E \right\}^2 \right)^{1/2}.
\end{aligned}$$

For a rectangular subdivision, the union of the patches $\tilde\omega_T$ covers Ω at most nine times, thus $\sum_{T\in\mathcal{T}_h} \|\nabla e\|_{\tilde\omega_T}^2 \le 9\|\nabla e\|^2$. Noting that $(a+b)^2 \le 2a^2+2b^2$ then leads to the following *residual estimator* error bound

$$\|\nabla(u-u_h)\| \le C(\beta_*) \left(\sum_{T\in\mathcal{T}_h} \left\{ h_T^2 \|R_T\|_T^2 + \sum_{E\in\mathcal{E}(T)} h_E \|R_E^*\|_E^2 \right\} \right)^{1/2}. \quad (1.108)$$

Remark 1.27. The combination of the interior residual and flux jump terms on the right-hand side of (1.108) can be used to define a simple *explicit* estimator $\bar\eta_T$, see [205]. In practice, the far superior accuracy of the local problem estimator (1.95) outweighs the computational cost incurred in solving the local problems (1.94) so the use of the cheaper estimator $\bar\eta_T$ in place of η_T is not recommended.

To show that the residual bound (1.108) implies the bound (1.101), we take the trivial bound $\|R_T\|_T \le \|R_T^0\|_T + \|R_T - R_T^0\|_T$, and exploit the fact that R_T^0 and R_E^* are piecewise constant to show that the terms $h_T^2 \|R_T^0\|_T^2$ and $h_E \|R_E^*\|_E^2$ on the right-hand side of (1.108) are individually bounded by η_T^2. The interior residual term is dealt with first. For $T\in\mathcal{T}_h$, we note that $R_T^0|_T \in \boldsymbol{P}_0$ and define $w_T = R_T^0\phi_T \in B_T \subset \mathcal{Q}_T$. It follows that

$$\begin{aligned}
\|R_T^0\|_T^2 = C(R_T^0, w_T)_T &= C(\nabla e_T, \nabla w_T)_T \quad (\text{setting } v = w_T \text{ in (1.94)}) \\
&\le C \|\nabla e_T\|_T \|\nabla w_T\|_T \\
&\le C \|\nabla e_T\|_T h_T^{-1} \|w_T\|_T \quad (\text{applying (1.104)}) \\
&\le C h_T^{-1} \|\nabla e_T\|_T \|R_T^0\|_T,
\end{aligned}$$

where in the last step we use the fact that $0 \leq \phi_T \leq 1$. This gives

$$h_T \left\| R_T^0 \right\|_T \leq C \left\| \nabla e_T \right\|_T . \tag{1.109}$$

The jump term is handled in the same way. For an interior edge, we define ω_E to be the union of the two elements adjoining edge $E \in \mathcal{E}(T)$, and define $w_E = R_E \psi_E \in Q_T \subset \mathcal{Q}_T$. From (1.94) we then have that

$$\|R_E^*\|_E^2 \leq C < R_E^*, w_E >_E \; = C \sum_{T' \subset \omega_E} \left[-(\nabla e_{T'}, \nabla w_E)_{T'} + (R_{T'}^0, w_E)_{T'} \right],$$

which, when combined with the scaling results $\|w_E\|_{T'} \leq h_E^{1/2} \|w_E\|_E$ and $\|\nabla w_E\|_{T'} \leq h_E^{-1/2} \|w_E\|_E$, leads to the desired bound

$$h_E^{1/2} \|R_E^*\|_E \leq C \sum_{T' \subset \omega_E} \|\nabla e_{T'}\|_{T'} . \tag{1.110}$$

Combining (1.109) and (1.110) with (1.108) then gives the upper bound (1.101) in Theorem 1.23.

The remaining issue is whether or not the estimated error η_T gives a lower bound on the local error. A precise statement is given below.

Proposition 1.28. *If the variational problem* (1.57) *is solved using a grid of bilinear rectangular elements, and if the rectangle aspect ratio condition is satisfied, then the estimator* $\eta_T \equiv \|\nabla e_T\|_T$ *computed via* (1.94) *using the approximation space* (1.97) *gives the bound*

$$\eta_T \leq C(\beta_{\omega_T}) \|\nabla(u - u_h)\|_{\omega_T} , \tag{1.111}$$

where ω_T *represents the patch of five elements that have at least one boundary edge* E *from the set* $\mathcal{E}(T)$.

Proof See Problem 1.23. □

To illustrate the usefulness of a posteriori error estimation, plots of the estimated error e_T associated with computed solutions u_h to the problems in Examples 1.1.3 and 1.1.4, are presented in Figures 1.20 and 1.21, respectively. The structure of the error can be seen to be very different in these two cases. Whereas the error distribution is a smooth function when solving Example 1.1.3, the effect of the singularity on the error distribution is very obvious in Figure 1.21. Moreover, comparing this error distribution, which comes from a uniform grid, with that in Figure 1.19 (derived from a stretched grid with the same number of degrees of freedom) clearly suggests that the most effective way of increasing accuracy at minimal cost is to perform local refinement in the neighborhood of the corner. These issues are explored further in Computational Exercise 1.4.

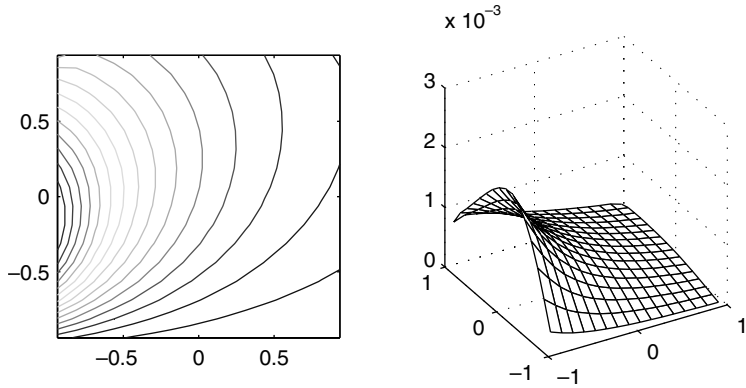

FIG. 1.20. Contour plot (left) and three-dimensional surface plot (right) of the estimated error associated with the finite element solution to Example 1.1.3 given in Figure 1.3.

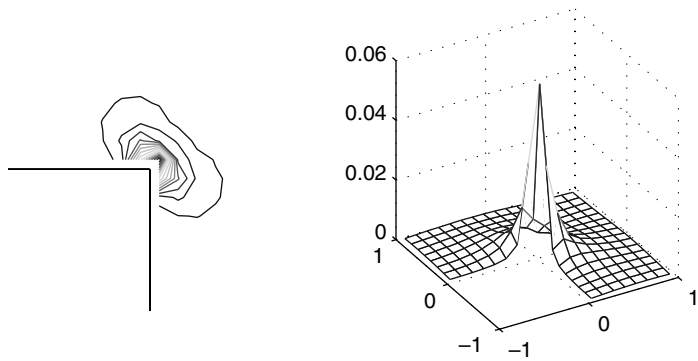

FIG. 1.21. Contour plot (left) and three-dimensional surface plot (right) of the estimated error associated with the finite element solution to Example 1.1.4 given in Figure 1.4.

1.6 Matrix properties

In this section, we describe some properties of the matrices arising from finite element discretization of the Poisson equation. These results will be used in the next chapter to analyze the behavior of iterative solution algorithms applied to the discrete systems of equations.

Let $\langle \mathbf{v}, \mathbf{w} \rangle = \mathbf{v}^T \mathbf{w}$ denote the Euclidean inner product on $\mathbb{R}^n$, with associated norm $\|\mathbf{v}\| = \langle \mathbf{v}, \mathbf{v} \rangle^{1/2}$. We begin with the observation that for *any* symmetric positive-definite matrix A of order n, the bilinear form given by

$$\langle \mathbf{v}, \mathbf{w} \rangle_A := \langle A\mathbf{v}, \mathbf{w} \rangle \tag{1.112}$$

defines an inner product on $\mathbb{R}^n$ with associated norm $\|\mathbf{v}\|_A = \langle \mathbf{v}, \mathbf{v} \rangle_A^{1/2}$. Given that A, the discrete Laplacian operator introduced in Section 1.3, is indeed symmetric and positive-definite, the inner product (1.112) and norm are well-defined in this case. Any vector $\mathbf{v} \in \mathbb{R}^n$ uniquely corresponds to a finite element function $v_h \in S_0^h$, and in particular there is a unique correspondence between the finite element solution u_h and the solution $\mathbf{u} = (\mathbf{u}_1, \mathbf{u}_2, \ldots, \mathbf{u}_n)^T$ to the matrix equation (1.21). If v_h and w_h are two functions in S_0^h, with coefficient vectors $\mathbf{v}$ and $\mathbf{w}$ respectively in $\mathbb{R}^n$, then the bilinear form derived from the Poisson equation, that is, $a(\cdot, \cdot)$ of (1.55), satisfies

$$a(v_h, w_h) = \int_\Omega \nabla v_h \cdot \nabla w_h = \langle \mathbf{v}, \mathbf{w} \rangle_A \,. \tag{1.113}$$

In simple terms, there is a one-to-one correspondence between the bilinear form $a(\cdot, \cdot)$ defined on the function space S_0^h, and the discrete inner product (1.112).

Recall from (1.22) that the discrete Laplacian can be viewed as the *Grammian matrix* of the basis $\{\phi_j\}$ associated with the inner product $a(\cdot, \cdot)$. It will also turn out to be useful to identify the Grammian with respect to the L_2-inner product,

$$Q = [q_{ij}], \qquad q_{ij} = \int_\Omega \phi_j \phi_i \,. \tag{1.114}$$

With this definition, it follows that for v_h, $w_h \in S_0^h$,

$$(v_h, w_h) = \langle Q\mathbf{v}, \mathbf{w} \rangle.$$

An immediate consequence is that Q is symmetric positive-definite, and the inner product $\langle \cdot, \cdot \rangle_Q$ defined by it constitutes a representation in $\mathbb{R}^n$ of the L_2-inner product in S_0^h. The matrix Q in (1.114) is referred to as the *mass matrix*.

The key property of the mass matrix is the following.

Proposition 1.29. *For $\boldsymbol{P}_1$ or $\boldsymbol{Q}_1$ approximation on a subdivision in $\mathbb{R}^2$ for which a shape regularity condition holds (as given in Definitions* 1.15 *and* 1.18*), the mass matrix Q approximates the scaled identity matrix in the sense that*

$$c\underline{h}^2 \leq \frac{\langle Q\mathbf{v}, \mathbf{v} \rangle}{\langle \mathbf{v}, \mathbf{v} \rangle} \leq Ch^2 \tag{1.115}$$

for all $\mathbf{v} \in \mathbb{R}^n$. Here $\underline{h} = \min_{\triangle_k \in \mathcal{T}_h} h_k$ and $h = \max_{\triangle_k \in \mathcal{T}_h} h_k$. The constants c and C are independent of both $\underline{h}$ and h.

Proof See Problem 1.24. □

The bound (1.115) can be further refined by making the assumption that the subdivision is *quasi-uniform*.

Definition 1.30 (Quasi-uniform subdivision). A sequence of triangular grids $\{\mathcal{T}_h\}$ is said to be *quasi-uniform* if there exists a constant $\rho > 0$ such that $\underline{h} \geq \rho h$ for every grid in the sequence.

For a quasi-uniform subdivision in $\mathbb{R}^2$ of shape regular elements, the bound (1.115) simplifies:

$$ch^2 \leq \frac{\langle Q\mathbf{v}, \mathbf{v}\rangle}{\langle \mathbf{v}, \mathbf{v}\rangle} \leq Ch^2 \quad \text{for all } \mathbf{v} \in \mathbb{R}^n. \tag{1.116}$$

Remark 1.31. If the subdivision is quasi-uniform, then the bound (1.116) holds for any degree of approximation, $\boldsymbol{P}_m$, $\boldsymbol{Q}_m$ with $m \geq 2$ (see Problem 1.25). However, the constants c and C depend on m.

The bound (1.116) depends on the spatial dimension. For tetrahedral or brick elements on a quasi-uniform discretization of a domain in $\mathbb{R}^3$, the corresponding bound is

$$ch^3 \leq \frac{\langle Q\mathbf{v}, \mathbf{v}\rangle}{\langle \mathbf{v}, \mathbf{v}\rangle} \leq Ch^3 \quad \text{for all } \mathbf{v} \in \mathbb{R}^n. \tag{1.117}$$

The mass matrix is a fundamental component of finite element analysis, arising naturally, for example, in the study of time-dependent problems. Here, however, it is only making a "cameo appearance" for the purposes of developing bounds on the eigenvalues of the discrete Laplacian A. The mass matrix will resurface later in Chapters 6 and 8.

One other property of the mass matrix will be useful in the next chapter. Given a Poisson problem (1.13), (1.14) and an approximation space S_E^h, the finite element solution u_h in S_E^h satisfying (1.19) is identical to that where the source function f is replaced by its projection $f_h \in S_0^h$ with respect to the L_2-norm. This is simply because f_h so defined satisfies $(f - f_h, w_h) = 0$ for every $w_h \in S_0^h$, so that

$$\int_\Omega \phi_i \, f_h = \int_\Omega \phi_i \, f \tag{1.118}$$

for each i, and thus there is no change in (1.23) when f_h is used instead of f. Note that if f_h in (1.118) is expressed in terms of the basis set $\{\phi_i\}_{i=1}^n$ then the coefficients are determined by solving the linear system $Q\mathbf{x} = \mathbf{f}$, where Q is the mass matrix, see Problem 1.26.

Another fundamental concept used for the analysis of matrix computations is the *condition number* of a matrix,

$$\kappa = \kappa(A) := \|A\| \, \|A^{-1}\|,$$

where the matrix norm is

$$\|A\| := \max_{\mathbf{v} \neq 0} \frac{\|A\mathbf{v}\|}{\|\mathbf{v}\|} \, .$$

When A is a symmetric positive-definite matrix, $\|A\| = \lambda_{\max}(A)$, the largest eigenvalue of A, and $\|A^{-1}\| = 1/\lambda_{\min}(A)$. Consequently, the condition number is

$$\kappa(A) = \lambda_{\max}(A)/\lambda_{\min}(A).$$

For direct solution methods, the size of the condition number is usually related to the number of accurate decimal places in a computed solution (see Higham [106]). In the next chapter, the convergence behavior of iterative solution methods will be precisely characterized in terms of $\kappa(A)$. In anticipation of this development, bounds on the condition number of the discrete Laplacian A are derived here. Two alternative approaches that can be used to establish such bounds will be described.

The first approach uses tools developed in Section 1.5 and is applicable in the case of arbitrarily shaped domains and non-uniform grids.

Theorem 1.32. *For $\boldsymbol{P}_1$ or $\boldsymbol{Q}_1$ approximation on a shape regular, quasi-uniform subdivision of $\mathbb{R}^2$, the Galerkin matrix A in* (1.21) *satisfies*

$$ch^2 \leq \frac{\langle A\mathbf{v}, \mathbf{v}\rangle}{\langle \mathbf{v}, \mathbf{v}\rangle} \leq C \quad \textit{for all } \mathbf{v} \in \mathbb{R}^n. \tag{1.119}$$

Here h is the length of the longest edge in the mesh or grid, and c and C are positive constants that are independent of h. In terms of the condition number, $\kappa(A) \leq C_* h^{-2}$ where $C_* = C/c$.

Proof Suppose that λ is an eigenvalue of A, that is, $A\mathbf{v} = \lambda\mathbf{v}$ for some eigenvector $\mathbf{v}$. Then $\lambda = \langle A\mathbf{v}, \mathbf{v}\rangle / \langle \mathbf{v}, \mathbf{v}\rangle$, and it follows that

$$\min_{\mathbf{v}\in\mathbb{R}^n} \frac{\langle A\mathbf{v}, \mathbf{v}\rangle}{\langle \mathbf{v}, \mathbf{v}\rangle} \leq \lambda \leq \max_{\mathbf{v}\in\mathbb{R}^n} \frac{\langle A\mathbf{v}, \mathbf{v}\rangle}{\langle \mathbf{v}, \mathbf{v}\rangle}\,. \tag{1.120}$$

For any $\mathbf{v} \in \mathbb{R}^n$, let v_h denote the corresponding function in S_0^h. The Poincaré-Friedrichs inequality (Lemma 1.2) implies that there is a constant c_Ω that is independent of the mesh parameter h such that

$$c_\Omega \|v_h\|^2 \leq \|\nabla v_h\|^2 = a(v_h, v_h)$$

for all $v_h \in S_0^h$. Rewriting in terms of matrices gives

$$c_\Omega \langle Q\mathbf{v}, \mathbf{v}\rangle \leq \langle A\mathbf{v}, \mathbf{v}\rangle \quad \text{for all } \mathbf{v} \in \mathbb{R}^n.$$

Combining the left-hand inequality of (1.116) and the characterization (1.120) shows that the smallest eigenvalue of A is bounded below by a quantity of order h^2.

For a bound on the largest eigenvalue of A, we turn to the local inverse estimate derived in Lemma 1.26, which states that for the restriction of v_h to an element T,

$$\|\nabla v_h\|_T^2 \leq C h_T^{-2} \|v_h\|_T^2\,.$$

Summing over all the elements and using the quasi-uniformity bound $h_T^{-1} \leq Ch^{-1}$ together with the right-hand inequality of (1.116) gives

$$\langle A\mathbf{v}, \mathbf{v}\rangle = a(v_h, v_h) \leq Ch^{-2}\|v_h\|^2 \leq C\,\langle \mathbf{v}, \mathbf{v}\rangle.$$

Thus, the bound on the largest eigenvalue is independent of h. □

Remark 1.33. The Galerkin matrix bound (1.119) holds for any degree of approximation, $\boldsymbol{P}_m$, $\boldsymbol{Q}_m$ with $m \geq 2$. The constants c and C depend on m.

Remark 1.34. With tetrahedral or brick elements on a quasi-uniform discretization of a domain in $\mathbb{R}^3$, the corresponding bound is

$$ch^3 \leq \frac{\langle A\mathbf{v}, \mathbf{v}\rangle}{\langle \mathbf{v}, \mathbf{v}\rangle} \leq Ch \quad \text{for all } \mathbf{v} \in \mathbb{R}^n. \tag{1.121}$$

This leads to an identical bound, $\kappa(A) \leq C_* h^{-2}$ on the condition number of the discrete Laplacian in arbitrary dimensions.

The second way of obtaining eigenvalue bounds is with Fourier analysis. This avoids the use of functional analytic tools, but the assumptions on the mesh are more restrictive than those expressed in Theorem 1.32.

A typical result is worked out in Problem 1.27. We use a double index notation to refer to the nodes ordered in a so-called "lexicographic" order as illustrated in Figure 1.22. Consider the concrete case of Example 1.1.1 discretized using $\boldsymbol{Q}_1$ approximation; Ω is a square of size $L = 2$, and a uniform $k \times k$ grid is used, so that the matrix dimension is $n = (k-1)^2$ with $k = L/h$. The analysis leads to the explicit identification of *all* of the eigenvalues:

$$\lambda^{(r,s)} = \frac{8}{3} - \frac{2}{3}\left(\cos\frac{r\pi}{k} + \cos\frac{s\pi}{k}\right) - \frac{4}{3}\cos\frac{r\pi}{k}\cos\frac{s\pi}{k}, \quad r, s = 1, \ldots, k-1 \tag{1.122}$$

together with the associated eigenvectors $\mathbf{U}^{(r,s)}$:

$$\mathbf{U}^{(r,s)}_{i,j} = \sin\frac{ri\pi}{k}\sin\frac{sj\pi}{k}, \tag{1.123}$$

where the index $i, j = 1, \ldots, k-1$ refers to the grid location.

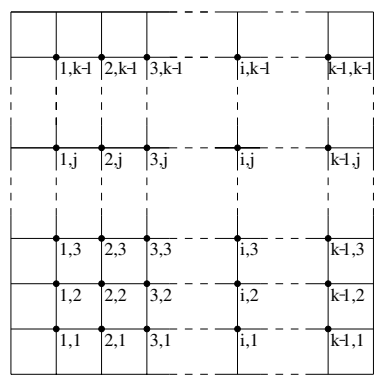

FIG. 1.22. Lexicographic ordering of node points with double index.

From (1.122), we see that the extreme eigenvalues of the $\boldsymbol{Q}_1$ discrete Laplacian are thus

$$\lambda_{\min} = \lambda^{(1,1)} = \frac{8}{3} - \frac{4}{3}\cos\frac{\pi}{k} - \frac{4}{3}\cos^2\frac{\pi}{k} = \frac{2\pi^2}{L^2}h^2 + \mathcal{O}(h^4),$$
$$\lambda_{\max} = \lambda^{(1,k-1)} = \lambda^{(k-1,1)} = \frac{8}{3} + \frac{4}{3}\cos^2\frac{\pi}{k} = 4 - \frac{4\pi^2}{3L^2}h^2 + \mathcal{O}(h^4),$$

and the condition number is

$$\kappa(A) = \frac{2L^2}{\pi^2}h^{-2} - \frac{1}{6} + \mathcal{O}(h^2). \tag{1.124}$$

Notice that the bound of Theorem 1.32 is tight in this case. (See also Computational Exercise 1.6.) Analogous estimates can also be established in the three-dimensional case, see Problem 1.28. Fourier analysis will be used in later chapters to give insight in other contexts, for example, to explore the convergence properties of multigrid methods (Section 2.5), and to investigate discrete approximations that exhibit high frequency oscillations in cases where the continuous solution is non-oscillatory (Section 3.5).

Problems

1.1. Show that the function $u(r,\theta) = r^{2/3}\sin((2\theta+\pi)/3)$ satisfies Laplace's equation expressed in polar coordinates;

$$\frac{\partial^2 u}{\partial r^2} + \frac{1}{r}\frac{\partial u}{\partial r} + \frac{1}{r^2}\frac{\partial^2 u}{\partial \theta^2} = 0.$$

1.2. Show that a solution u satisfying the Poisson equation and a mixed condition $\alpha u + \frac{\partial u}{\partial n} = 0$ on the boundary $\partial\Omega$, where $\alpha > 0$ is a constant, also satisfies the following weak formulation: find $u \in \mathcal{H}^1(\Omega)$ such that

$$\int_\Omega \nabla u \cdot \nabla v + \alpha \int_{\partial\Omega} u\, v = \int_\Omega v f \quad \text{for all } v \in \mathcal{H}^1(\Omega).$$

Show that $c(u,v) := \int_\Omega \nabla u \cdot \nabla v + \alpha \int_{\partial\Omega} uv$ defines an inner product over $\mathcal{H}^1(\Omega)$, and hence establish that a solution of the weak formulation is uniquely defined.

1.3. Construct the $\boldsymbol{P}_2$ basis functions for the element with vertices $(0,0)$, $(1,0)$ and $(0,1)$ illustrated in Figure 1.7.

1.4. For the pair of elements illustrated, show that the bilinear function that takes on the value one at vertex P and zero at the other vertices gives different values at the midpoint M on the common edge (and is hence discontinuous).

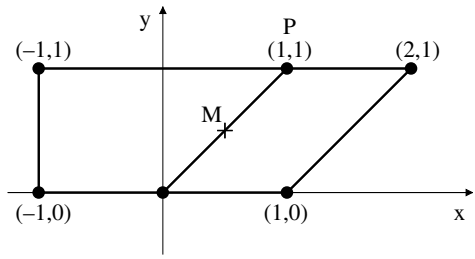

Show that the corresponding isoparametrically mapped bilinear function (defined via (1.26) and (1.27)) is continuous along the common edge.

1.5. By substituting (1.36) into (1.45), show that the $\boldsymbol{P}_1$ stiffness matrix is given by

$$A_k(i,j) = \frac{1}{4|\triangle_k|}(b_i b_j + c_i c_j),$$

where b_i and c_i, $i = 1, 2, 3$ are defined in (1.43).

1.6. A generic point P in a triangle is parameterized by three triangular (or *barycentric*) coordinates L_1, L_2 and L_3, which are simple ratios of the triangle areas illustrated $(L_1, L_2, L_3) \equiv (|\triangle_{3P2}|/|\triangle|, |\triangle_{1P3}|/|\triangle|, |\triangle_{2P1}|/|\triangle|)$.

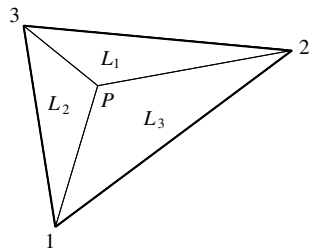

By construction, show that

$$L_i = \frac{1}{2|\triangle|}(a_i + b_i x + c_i y),$$

where a_i satisfies $\sum_{i=1}^{3} a_i = 2|\triangle|$, and b_i and c_i are given by (1.43). Check that the functions L_i are linear nodal basis functions (so that $L_i \equiv \psi_{k,i}$, see Section 1.4.1), and hence verify the formula for the $\boldsymbol{P}_1$ stiffness matrix given in Problem 1.5.

1.7. Show that the determinant of the $\boldsymbol{Q}_1$ Jacobian matrix (1.48) is a linear function of the coordinates (ξ, η). Verify that the $\boldsymbol{Q}_1$ Jacobian (1.48) is a constant matrix if the mapped element is a parallelogram.

1.8. Show that the $\boldsymbol{Q}_1$ Jacobian (1.48) is a diagonal matrix if the mapped element is a rectangle aligned with the coordinate axes. Compute the $\boldsymbol{Q}_1$ stiffness

matrix in this case (assume that the horizontal and vertical sides are of length hx and hy, respectively).

1.9. Given the Gauss points $\xi_s = \pm 1/\sqrt{3}$ and $\eta_t = \pm 1/\sqrt{3}$ as illustrated in Figure 1.15, show that if f is bilinear, that is, $f(\xi, \eta) = (a + b\xi)(c + d\eta)$ where a, b, c and d are constants, then

$$\int_{-1}^{1}\int_{-1}^{1} f \mathrm{d}\xi \mathrm{d}\eta = \sum_s \sum_t f(\xi_s, \eta_t).$$

1.10. Show that if $\int_{\partial\Omega_D} \mathrm{ds} \neq 0$ then the bilinear form $a(\cdot, \cdot)$ in (1.55) defines an inner product over the space $\mathcal{H}^1_{E_0} \times \mathcal{H}^1_{E_0}$.

1.11. Show that, if u and u_h satisfy (1.56) and (1.57) respectively in the case of zero Dirichlet data (so that $\mathcal{H}^1_E = \mathcal{H}^1_{E_0}$), then the error in energy satisfies

$$\|\nabla(u - u_h)\|^2 = \|\nabla u\|^2 - \|\nabla u_h\|^2 .$$

1.12. Given a square domain $\Omega = [0, L] \times [0, L]$, show that

$$\int_\Omega u^2 \leq \frac{L^2}{2} \int_\Omega \left(\left| \frac{\partial u}{\partial x} \right|^2 + \left| \frac{\partial u}{\partial y} \right|^2 \right)$$

for any function $u \in \mathcal{H}^1(\Omega)$ that is zero everywhere on the boundary. (Hint: $u(x, y) = u(0, y) + \int_0^x \frac{\partial u}{\partial x}(\xi, y)\, \mathrm{d}\xi$.)

1.13. Prove Proposition 1.6. (Hint: use the definition (1.63).)

1.14. Let V_h be a finite element subspace of $V := \mathcal{H}^1(\Omega)$. Define a bilinear form $a(\cdot, \cdot)$ on $V \times V$, and let $u \in V$ and $u_h \in V_h$ satisfy

$$\begin{aligned} a(u, v) &= (f, v) \quad && \text{for all } v \in V \\ a(u_h, v_h) &= (f, v_h) \quad && \text{for all } v_h \in V_h \end{aligned}$$

respectively. If there exist positive constants γ and Γ such that

$$\begin{aligned} a(v, v) &\geq \gamma \|v\|^2_{1,\Omega} && \text{for all } v \in V \\ |a(u, v)| &\leq \Gamma \|u\|_{1,\Omega} \|v\|_{1,\Omega} && \text{for all } u, v \in V, \end{aligned}$$

show that there exists a positive constant $C(\gamma, \Gamma)$ such that

$$\|u - u_h\|_{1,\Omega} \leq C \inf_{v_h \in V_h} \|u - v_h\|_{1,\Omega} .$$

1.15. For any function $w(x)$ defined on $[0, 1]$, let Πw be the linear interpolant satisfying $\Pi w(0) = w(0)$ and $\Pi w(1) = w(1)$. Use Rolle's theorem to show that

$e = w - \Pi w$ satisfies

$$\int_0^1 (e')^2 \mathrm{d}x \leq \frac{1}{2} \int_0^1 (e'')^2 \mathrm{d}x.$$

1.16. Prove Proposition 1.14. (Hint: use simple trigonometric identities.)

1.17. Prove Proposition 1.16.

1.18. Prove Proposition 1.17. (Hint: follow the proofs of Lemma 1.11 and Lemma 1.13.)

1.19. Prove Proposition 1.22. (Hint: do Problem 1.18 first.)

1.20. Given that $u \in \mathcal{H}^s(\Omega) \Leftrightarrow \|D^s u\| < \infty$, show that the function $u(r, \theta) = r^{2/3} \sin((2\theta + \pi)/3)$ defined on the pie-shaped domain Ω where $0 \leq r \leq 1$ and $-\pi/2 \leq \theta \leq \pi$ is in $\mathcal{H}^1(\Omega)$, but is not in $\mathcal{H}^2(\Omega)$.

1.21. Show that if $\mathcal{Q}_T$ is the space (1.97) of edge and bubble functions then there exists a unique solution to the local problem (1.94).

1.22. Show that the inverse estimate (1.104) holds in the case of a rectangular element T.

1.23. Prove Proposition 1.28. (Hint: take $v = e_T$ in the local problem (1.94), and then choose w_T and w_E as in the proof of Theorem 1.23 with a view to separately bounding the interior and jump residual terms by $\|\nabla(u - u_h)\|_T$.)

1.24. Prove Proposition 1.29. (Hint: given that Q is the mass matrix (1.114) and that $u_h = \sum_{j=1}^n \mathbf{u}_j \phi_j$ is a finite element function on $\Omega \subset \mathbb{R}^2$, show that $\|u_h\|_\Omega^2 = \langle Q\mathbf{u}, \mathbf{u}\rangle$. Write $\langle Q\mathbf{u}, \mathbf{u}\rangle = \sum_{k \in \mathcal{T}_h} \langle Q^{(k)} \mathbf{v}_k, \mathbf{v}_k\rangle$ where $Q^{(k)}$ is the element mass matrix for element k, that is, $Q^{(k)} = [q_{ij}]$ with $q_{ij} = \int_{\Delta_k} \phi_j \phi_i$. Then prove that for a shape regular element, $\underline{c} h_k^2 \langle \mathbf{v}_k, \mathbf{v}_k\rangle \leq \langle Q^{(k)} \mathbf{v}_k, \mathbf{v}_k\rangle \leq \bar{c} h_k^2 \langle \mathbf{v}_k, \mathbf{v}_k\rangle$ for all functions $\mathbf{v}_k$.)

1.25. Prove that the mass matrix bound (1.116) holds for $\boldsymbol{Q}_2$ approximation on a uniform grid of square elements.

1.26. For any $f \in L_2(\Omega)$, let f_h be the L_2 projection into S_0^h. Writing $f_h = \sum_{j=1}^n \bar{\mathbf{f}}_j \phi_j$, show that the coefficient vector $\bar{\mathbf{f}} = (\bar{\mathbf{f}}_1, \bar{\mathbf{f}}_2, \ldots, \bar{\mathbf{f}}_n)^T$ is the solution of

$$Q\bar{\mathbf{f}} = \mathbf{f},$$

where Q is the mass matrix (1.114) and $\mathbf{f} = [\boldsymbol{f}_i]$ with $\boldsymbol{f}_i = \int_\Omega \phi_i f$.

1.27. In the double index notation indicated by Figure 1.22 and with $\mathbf{U}_{i,j}$ denoting the value of u_h at the lattice point i, j, the Galerkin system of equations

derived from $\boldsymbol{Q}_1$ approximation on a uniform square grid can be written as

$$\frac{8}{3}\mathbf{U}_{i,j} - \frac{1}{3}\mathbf{U}_{i+1,j+1} - \frac{1}{3}\mathbf{U}_{i+1,j} - \frac{1}{3}\mathbf{U}_{i+1,j-1} - \frac{1}{3}\mathbf{U}_{i,j+1} - \frac{1}{3}\mathbf{U}_{i,j-1} - \frac{1}{3}\mathbf{U}_{i-1,j+1} - \frac{1}{3}\mathbf{U}_{i-1,j} - \frac{1}{3}\mathbf{U}_{i-1,j-1} = h^2\mathbf{f}_{i,j}$$

with $\mathbf{U}_{k,j}, \mathbf{U}_{0,j}, \mathbf{U}_{i,0}, \mathbf{U}_{i,k}$ given by the Dirichlet boundary condition. The eigenvalues $\lambda^{r,s}$ of the Galerkin matrix therefore satisfy

$$\frac{8}{3}\mathbf{U}^{r,s}_{i,j} - \frac{1}{3}\mathbf{U}^{r,s}_{i+1,j+1} - \frac{1}{3}\mathbf{U}^{r,s}_{i+1,j} - \frac{1}{3}\mathbf{U}^{r,s}_{i+1,j-1} - \frac{1}{3}\mathbf{U}^{r,s}_{i,j+1} - \frac{1}{3}\mathbf{U}^{r,s}_{i,j-1} - \frac{1}{3}\mathbf{U}^{r,s}_{i-1,j+1} - \frac{1}{3}\mathbf{U}^{r,s}_{i-1,j} - \frac{1}{3}\mathbf{U}^{r,s}_{i-1,j-1} = \lambda^{r,s}\,\mathbf{U}^{r,s}_{i,j}$$

for $r, s = 1, \ldots, k-1$. Verify that the vector $\mathbf{U}^{r,s}$ with entries

$$\mathbf{U}^{r,s}_{i,j} = \sin\frac{ri\pi}{k}\sin\frac{sj\pi}{k}, \quad i,j = 1,\ldots,k-1$$

is an eigenvector for arbitrary $r, s = 1, \ldots, k-1$, and hence that the corresponding eigenvalue is

$$\lambda^{r,s} = \frac{8}{3} - \frac{2}{3}\left(\cos\frac{r\pi}{k} + \cos\frac{s\pi}{k}\right) - \frac{4}{3}\cos\frac{r\pi}{k}\cos\frac{s\pi}{k}, \quad r,s = 1,\ldots,k-1.$$

1.28. In triple index notation with $\mathbf{U}_{i,j,k}$ denoting the value of u_h at the lattice point i, j, k, $i = 1, \ldots, l-1$, $j = 1, \ldots, l-1$, $k = 1, \ldots, l-1$ show that the Galerkin system derived from trilinear approximation of the Poisson equation with Dirichlet boundary conditions on a uniform grid of cube elements with side length h can be written as

$$\begin{aligned}
&\frac{8h}{3}\mathbf{U}_{i,j,k} - \frac{h}{6}\left(\mathbf{U}_{i,j+1,k-1} + \mathbf{U}_{i,j-1,k-1} + \mathbf{U}_{i+1,j,k-1} + \mathbf{U}_{i-1,j,k-1}\right)\\
&\quad - \frac{h}{12}\left(\mathbf{U}_{i+1,j+1,k-1} + \mathbf{U}_{i+1,j-1,k-1} + \mathbf{U}_{i-1,j+1,k-1} + \mathbf{U}_{i-1,j-1,k-1}\right)\\
&\quad - \frac{h}{6}\left(\mathbf{U}_{i+1,j+1,k} + \mathbf{U}_{i+1,j-1,k} + \mathbf{U}_{i-1,j+1,k} + \mathbf{U}_{i-1,j-1,k}\right)\\
&\quad - \frac{h}{12}\left(\mathbf{U}_{i+1,j+1,k+1} + \mathbf{U}_{i+1,j-1,k+1} + \mathbf{U}_{i-1,j+1,k+1} + \mathbf{U}_{i-1,j-1,k+1}\right)\\
&\quad - \frac{h}{6}\left(\mathbf{U}_{i,j+1,k+1} + \mathbf{U}_{i,j-1,k+1} + \mathbf{U}_{i+1,j,k+1} + \mathbf{U}_{i-1,j,k+1}\right) = h^2\mathbf{f}_{i,j,k}
\end{aligned}$$

for $i, j, k = 1, \ldots, l-1$ with $\mathbf{U}_{i,j,k}$ given by the Dirichlet boundary conditions when any of i, j or k is 0 or l.

1.29. This builds on Problems 1.27 and 1.28. Show that

$$\mathbf{U}^{r,s,t}_{i,j,k} = \sin\frac{ri\pi}{l}\sin\frac{sj\pi}{l}\sin\frac{tk\pi}{l}, \quad i,j,k = 1,\ldots,l-1$$

is an eigenvector of the Galerkin matrix in Problem 1.28 for $r, s, t = 1, \ldots, l-1$, and that the eigenvalues $\lambda^{r,s,t}$ satisfying

$$\begin{aligned}
&\frac{8h}{3}\mathbf{U}^{r,s,t}_{i,j,k} - \frac{h}{6}\left(\mathbf{U}^{r,s,t}_{i,j+1,k-1} + \mathbf{U}^{r,s,t}_{i,j-1,k-1} + \mathbf{U}^{r,s,t}_{i+1,j,k-1} + \mathbf{U}^{r,s,t}_{i-1,j,k-1}\right)\\
&\quad - \frac{h}{12}\left(\mathbf{U}^{r,s,t}_{i+1,j+1,k-1} + \mathbf{U}^{r,s,t}_{i+1,j-1,k-1} + \mathbf{U}^{r,s,t}_{i-1,j+1,k-1} + \mathbf{U}^{r,s,t}_{i-1,j-1,k-1}\right)\\
&\quad - \frac{h}{6}\left(\mathbf{U}^{r,s,t}_{i+1,j+1,k} + \mathbf{U}^{r,s,t}_{i+1,j-1,k} + \mathbf{U}^{r,s,t}_{i-1,j+1,k} + \mathbf{U}^{r,s,t}_{i-1,j-1,k}\right)\\
&\quad - \frac{h}{12}\left(\mathbf{U}^{r,s,t}_{i+1,j+1,k+1} + \mathbf{U}^{r,s,t}_{i+1,j-1,k+1} + \mathbf{U}^{r,s,t}_{i-1,j+1,k+1} + \mathbf{U}^{r,s,t}_{i-1,j-1,k+1}\right)\\
&\quad - \frac{h}{6}\left(\mathbf{U}^{r,s,t}_{i,j+1,k+1} + \mathbf{U}^{r,s,t}_{i,j-1,k+1} + \mathbf{U}^{r,s,t}_{i+1,j,k+1} + \mathbf{U}^{r,s,t}_{i-1,j,k+1}\right) = \lambda^{r,s,t}\,\mathbf{U}^{r,s,t}_{i,j,k}
\end{aligned}$$

are therefore

$$\begin{aligned}
\lambda^{r,s,t} =& \frac{8h}{3} - \frac{2h}{3}\left(\cos\frac{r\pi}{l}\cos\frac{s\pi}{l} + \cos\frac{r\pi}{l}\cos\frac{t\pi}{l} + \cos\frac{s\pi}{l}\cos\frac{t\pi}{l}\right)\\
&- \frac{2h}{3}\cos\frac{r\pi}{l}\cos\frac{s\pi}{l}\cos\frac{t\pi}{l}, \quad r, s, t = 1, \ldots, l-1.
\end{aligned}$$

Computational exercises

Two specific domains are built into IFISS by default, $\Omega_\square \equiv (-1,1)\times(-1,1)$ and $\Omega_\lrcorner \equiv \Omega_\square \backslash \{(-1,0)\times(-1,0)\}$. Numerical solutions to a Dirichlet problem defined on $\Omega_\square$ or $\Omega_\lrcorner$ can be computed by running `square_diff` or `ell_diff` as appropriate, with source data f and boundary data g specified in function m-files `../diffusion/specific_rhs` and `../diffusion/specific_bc`, respectively. Running the driver `diff_testproblem` sets up the data files `specific_rhs` and `specific_bc` associated with the reference problems in Examples 1.1.1–1.1.4.

1.1. Consider Example 1.1.1 with a typical solution illustrated in Figure 1.1. Evaluating the series solution (1.5) the maximum value of u is given by $u(0,0) = 0.294685413126$. Tabulate a set of computed approximations $u_h(0,0)$ to $u(0,0)$ using uniform 8×8, 16×16 and 32×32 grids with bilinear and biquadratic approximation. Then, by computing $|u(0,0) - u_h(0,0)|$, estimate the order of convergence that is achieved in each case.

1.2. Consider Example 1.1.2 with a typical solution illustrated in Figure 1.2. Tabulate a set of computed approximations u^*_h to the (unknown) maximum value of u^* using a sequence of uniform grids. By comparing successive approximations $|u^*_h - u^*_{h/2}|$, estimate the order of convergence that is achieved using bilinear and biquadratic approximation.

1.3. Write a function that postprocesses a $\boldsymbol{Q}_1$ solution, u_h, and computes the global error $\|\nabla(u - u_h)\|$ for the analytic test problem in Example 1.1.3. Hence,

verify the results given in Table 1.4. Then use your function to generate a table of estimated and exact errors for the set of stretched element grids that is automatically generated by IFISS.

1.4. Consider Example 1.1.2 with a typical solution illustrated in Figure 1.2. Tabulate the estimated error η for a sequence of uniform square grids, and hence estimate the order of convergence. Then change the source function from $f = 1$ to $f = xy$ and repeat the experiment. Can you explain the difference in the order of convergence?

1.5. Quadrilateral elements are also built into IFISS. Specifically, the function `quad_diff` can be used to solve problems defined on general quadrilateral domains with a Neumann condition on the right-hand boundary. By setting the source function to unity and the Dirichlet boundary data to zero, the effect of geometry on models of the deflection of an elastic membrane stretched over the bow-tie shaped domain illustrated below can be explored. (The Neumann condition acts as a symmetry condition, so only half of the bow-tie needs to be considered.)

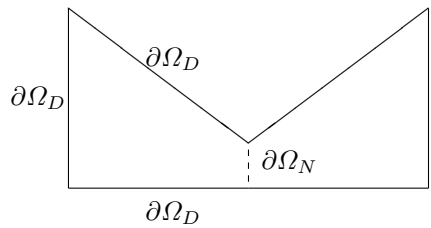

1.6. Using the matlab `eig` function, compute the eigenvalues of the coefficient matrix for Example 1.1.1 with $k = 8$ using $\boldsymbol{Q}_1$ approximation on a uniform grid, and verify that there are $(k-1)^2$ eigenvalues given by the analytic expression (1.122) together with $4k$ eigenvalues of unity (corresponding to the Dirichlet boundary nodes). Then, use the matlab `eigs` function to compute the maximum and minimum eigenvalues of the $\boldsymbol{Q}_1$ stiffness matrix on a sequence of uniformly refined grids, and verify that the condition number grows like $8/(\pi^2 h^2)$ in the limit $h \to 0$.